EI SEVIER

Contents lists available at ScienceDirect

International Journal of Plasticity

journal homepage: www.elsevier.com/locate/ijplas



Towards a greater understanding of serrated flows in an Alcontaining high-entropy-based alloy



J. Brechtl^a, S.Y. Chen^{b,**}, X. Xie^b, Y. Ren^c, J.W. Qiao^d, P.K. Liaw^{b,*}, S.J. Zinkle^{a,b,e}

- ^a The Bredesen Center for Interdisciplinary Research and Education, The University of Tennessee, Knoxville, TN, 37996, USA
- b Department of Materials Science and Engineering, The University of Tennessee, Knoxville, TN, 37996, USA
- ^cX-ray Science Division, Argonne National Laboratory, Argonne, IL, 60439, USA
- ^d College of Materials Science and Engineering, Taiyuan University of Technology, China
- ^e Department of Nuclear Engineering, The University of Tennessee, Knoxville, TN, 37996, USA

ARTICLE INFO

Keywords: High entropy alloys Dislocations Serrated flow Mechanical testing Numerical algorithms

ABSTRACT

A serrated flow, which occurs in a material undergoing mechanical deformation, is a complex process of great engineering significance. Here statistical, dynamical, and multifractal modeling and analyses were performed on the stress-time series to characterize and model the stress-drop behavior of an Al_{0.5}CoCrCuFeNi high-entropy alloy (HEA). Results indicate that the spatiotemporal dynamics of the serrated flow is affected by changes in the strain rate and test temperature. The sample entropy, in general, was found to be the highest in the samples tested at 500 °C. The higher complexity in the serrated flow at this temperature appeared to be associated with the stress-drop behavior that had intermediate values in terms of the maximum stress drop, the multifractality of the data set, and the histogram distributions. Moreover, the sample entropy was the lowest for the samples tested at 600 °C. The lower complexity values were associated with a wider multifractal spectrum and a less uniform and sparser distribution of the stress-drop magnitudes. In terms of the serration types, Type-C serrations were related to the lowest complexity values, widest multifractal spectra, and higher probability of exhibiting larger stress drops. Conversely, Type-A and B serrations were associated with the higher complexity, narrower spectra, and lower probability of higher stress drops. Furthermore, the body-centered-cubic (BCC) structure and the fully-ordered L12 nano-particles were found to emerge in the samples at 600 °C and are thought to be linked to the decreased spatiotemporal correlations in the stressdrop behavior.

1. Introduction

High-entropy alloys (HEAs), which are a type of complex concentrated alloy (Cantor et al., 2004; Miracle and Senkov, 2017; Yeh et al., 2004b; Zhang et al., 2014; Zhang et al., 2017), are an important class of materials that were developed in the early-2000s. In terms of compositions, they have been defined as being comprised of five or more principal elements in which the principal elements may have an atomic concentration between 35 and 5 atomic percent (at.-%) (Hsu et al., 2010; Miracle, 2017; Yeh et al., 2004a, 2004b; Zhang et al., 2014; Zhang et al., 2017). Furthermore, when the material undergoes the elemental segregation, precipitation, chemical ordering, and spinodal decomposition, a significant amount of disorder remains (Santodonato et al., 2015). A consequence

E-mail addresses: schen38@vols.utk.edu (S.Y. Chen), pliaw@utk.edu (P.K. Liaw).

^{*} Corresponding author.

^{**} Corresponding author.

of having a high mixing entropy is the favor of disordered solid solutions at higher temperatures (Cantor et al., 2004; Zhang et al., 2014). Recently, Miracle et al. showed that enthalpy plays a critical role in determining which compositions form single solid-solution phases with no long-range configurational order (Miracle and Senkoy, 2017; Santodonato et al., 2018).

In addition to their unique microstructure, HEAs also possess superior properties. These properties include high strength and fracture toughness (Cai et al., 2017; Gao et al., 2017; Gludovatz et al., 2014; Koch, 2017; Lee et al., 2018; Lilensten et al., 2018), remarkable resistance to shear failure (Li et al., 2017b), good corrosion resistance (Chou et al., 2010; Kao et al., 2017; Nair et al., 2018; Shi et al., 2017a, 2017b, 2018a, 2018b; Tang et al., 2014), comparable or higher fatigue resistance (Chen et al., 2018a; Hemphill et al., 2012; Liu et al., 2019b; Seifi et al., 2015; Tang et al., 2015; Thurston et al., 2017), outstanding wear resistance (Chen et al., 2018c: Chuang et al., 2011, 2013), and excellent cryogenic tensile and fracture properties (Gludovatz et al., 2014; Jo et al., 2017; Li et al., 2017a; Liu et al., 2019b; Lyu et al., 2018; Qiao et al., 2011). Furthermore, HEAs have shown that they exhibit the decent irradiation stability (Egami et al., 2014; He et al., 2016; Kumar et al., 2016; Xia et al., 2015a, 2015b, 2016; Yang et al., 2018b; Zhang et al., 2015).

During mechanical testing, an alloy may experience the jerky motion that is characterized by fluctuations in its stress-strain graph. This type of inhomogeneous deformation is known as the serrated flow and is observed as a sudden drop in the applied stress in a short amount of time or as a mix of increasing and decreasing stress levels. Serration behavior is significant because it is typically associated with plastic instabilities and substantial changes in the microstructure (Neuhauser, 1993; Niu et al., 2017; Zhang et al., 2014, 2017). This type of mechanical behavior has been observed in various material systems (Zhang et al., 2014, 2017), including steels (Field and Aken, 2018; Lan and Zhang, 2018; Madivala et al., 2018; Sarkar et al., 2015; Yang et al., 2018a; Zavattieri et al., 2009; Zhang et al., 2017), Al-Mg alloys (Chatterjee et al., 2009; Chibane et al., 2017; Jobba et al., 2015; Sarkar et al., 2010; Shibkov et al., 2016; Valdes-Tabernero et al., 2017; Yuzbekova et al., 2017; Zhang et al., 2017), Al alloys (Benallal et al., 2008; Zhang et al., 2017), HEAS (Carroll et al., 2015; Chen et al., 2014, 2015, 2016, 2018b, 2018d; Hu et al., 2018; Komarasamy et al., 2016; Liu et al., 2019a; Tong et al., 2005; Zhang et al., 2014, 2017), and bulk metallic glasses (Antonaglia et al., 2014a, 2014b; Jiang et al., 2008; Li et al., 2016; Maaß et al., 2011; Shi et al., 2018c; Torre et al., 2010; Zhang et al., 2017).

In bulk metallic glasses, the serrated plastic flow is attributed to shear-banding dynamics (Antonaglia et al., 2014b; Li et al., 2016; Song et al., 2017; Zhang et al., 2017). In crystalline materials, serrations are typically caused by the locking of dislocations by solute atoms, which corresponds to the so-called dynamic strain ageing (DSA) (Chen et al., 2015; Sarkar et al., 2015; Yilmaz, 2011; Zhang et al., 2014, 2017). Another study found that the γ precipitates enhance the serrated flow behavior, by acting as additional obstacles to mobile dislocations and promoting solute atoms aggregating around the moving dislocations (Cai et al., 2015). Tabachnikova et al. found that dendrite boundaries and sigma-phase particles could act as the barriers for the mobile dislocations, resulting in serrations (Tabachnikova et al., 2017). Twinning was also found to be a contributor to the serrated flow by hindering dislocation motion at twin boundaries (Liu et al., 2019b; Lyu et al., 2018; Madivala et al., 2018; Zavattieri et al., 2009; Zhang et al., 2014, 2017). Furthermore, interactions between dislocations or twins with different orientations also result in the serrated flow (Zhang et al., 2017). Finally, another important feature of the serrated flow is the development and propagation of localized deformation bands (Hahner et al., 2002).

Chen et al., 2018d). Here they found that after testing at 500 °C and 600 °C, there were $L1_2$ nano-particles in the matrix, as observed under the transmission electron microscopy. They surmised that during compression, the $L1_2$ particles may provide an obstacle for the moving dislocations, which cause them to be pinned by the mobile solute atoms, leading to the observed serrations. In a previous study, it was found that the emergence of the B2 phase in the alloy during testing at 600 °C may also alter the characteristic behavior of the serrated flow (Chen et al., 2015).

Other studies have implied that Al plays a crucial role in the interaction between solute atoms and dislocations in the Alcontaining HEAs (Niu et al., 2017; Yasuda et al., 2015). Yasuda et al. compared the mechanical behavior of $Al_{0.3}$ CoCrFeNi and CoCrFeNi HEAs (Yasuda et al., 2015). Here, they found that the Al-containing HEA exhibited serrations, while the latter specimen did not. From their results, they surmised that the Al atoms play an important role in the dynamic strain aging (DSA) of the material. The researchers also concluded that the DSA arises because of the creation of Al-containing solute atmospheres near a moving dislocation core, leading to an increase of the frictional stress on the dislocations. Experiments performed by Niu et al. involving $Al_{0.5}$ CoCrFeNi and CoCrFeNi HEAs found similar results (Niu et al., 2017).

Serrations may exhibit different characteristics, depending on the applied strain rate or test temperature (Antonaglia et al., 2014b; Carroll et al., 2015; Zhang et al., 2014, 2017). During DSA, for example, a serrated flow typically undergoes three types of serrations that have been labelled as A, B, and C (Carroll et al., 2015; Rodriguez, 1984; Zhang et al., 2014, 2017). Type-A serrations rise above the general level of stress values before experiencing a stress drop, and are periodic in nature. This type is associated with high strain rates and continuous band propagation with a high degree of spatial correlation. Type-B serrations fluctuate about the general level of stresses in a more rapid manner and occur with less correlations than Type-A. Type-C serrations, on the other hand, contain stress drops that occur below the general level of stresses and are associated with weak spatial correlations. Fig. 1 presents a schematic representation (Carroll et al., 2015) of the three serration types, as discussed above.

Several different types of modeling and analysis have been used as an attempt to quantify the serrated flow in fundamentally-different alloy systems. These techniques include complexity (Sarkar et al., 2007, 2010, 2015), multifractal (Bharathi et al., 2001; Lebedkina and Lebyodkin, 2008; Lebedkina et al., 2014; Lebyodkin and Lebedkina, 2008), and statistical (Antonaglia et al., 2014a, 2014b; Carroll et al., 2015; Chatterjee et al., 2009; Chen et al., 2014, 2015, 2016, 2018d; Friedman et al., 2012; Lebedkina and Lebyodkin, 2008; Li et al., 2016; Uhl et al., 2015; Zhang et al., 2014, 2017) modeling and analysis.

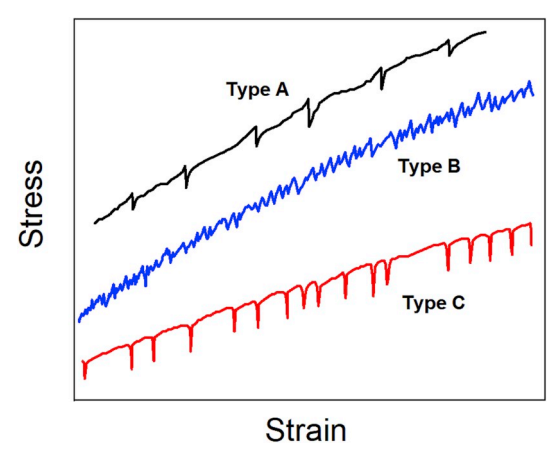


Fig. 1. Types A, B, and C serrations (Carroll et al., 2015). (For the interpretation of the references to color in this figure legend, the reader is referred to the Web version of this article.)

The above methods have been used to model and analyze the serrated flow because it is thought that serration curves contain scaling laws, self-similarity, and complex dynamics. Since a similar weakening effect is observed in conventional materials with dynamic-strain aging, where solute atoms diffuse and stick to dislocations, thereby pinning them in place (Carroll et al., 2015), it is believed that the conventional interpretations can apply to this material system. For example, the serrated flow in HEAs and other alloys transition from Types A to C serrations, when the temperature is increased within a certain range of values (Carroll et al., 2015). Also, there is a critical strain in which different serrations types can occur (Chen et al., 2018d). Additionally, as discussed by Chen et al., the critical strain observed in $Al_{0.5}$ CoCrCuFeNi HEA was found to decrease with increasing the temperature from 300 °C to 600 °C. Importantly, this decreasing trend has been observed in other material systems as well, such as superalloy IN738LC (Sharghi-Moshtaghin and Asgari, 2008).

For a previous investigation on the serrated flow in the alloy studied for this project, please see the work conducted by Chen et al. (2015). In the present study, the serration behavior of the $Al_{0.5}$ CoCrCuFeNi HEA, while undergoing compression tests, was modeled and analyzed, using the methods described above. The current work can be thought of as innovative since it applies methods, which have not been used before to study the serrated flow in HEAs. Furthermore, it is hoped that through the current work, a more universal understanding behind the serrated flow of this material system will be achieved. Therefore, it is anticipated that the current work will advance our fundamental understanding of the serration phenomena in HEAs, while laying the groundwork for future investigations of a similar nature.

2. Experimental

In the present investigation, the compression behavior of the ${\rm Al}_{0.5}{\rm CoCrCuFeNi}$ (in mole percent) HEA was examined. Here, the studied alloy was prepared by arc-melting a combination of principal elements with purities > 99.9 (weight percent) in a Ti-gettered high-purity argon atmosphere. To achieve the high uniformity of specimens, the process of melting and solidification was repeated at a minimum of 5 times. After the above process, the molten alloy was drop-cast into a water-cooled copper mold that was 2 mm in diameter

All test specimens were of a cylindrical geometry with 2 mm in diameter and 4 mm in length, i.e., an aspect ratio (length vs. diameter) of 2:1. The lateral surface was polished, using a Buehler rotating/grinder polishing system. Moreover, the top and bottom surfaces of the samples were carefully polished to ensure that both sides were parallel to each other before the compression tests.

The compression experiments utilized a material test system (MTS) servohydraulic-testing machine. Samples were compressed at strain rates of 5×10^{-5} , 2×10^{-4} , and 2×10^{-3} s⁻¹ and test temperatures of $400\,^{\circ}$ C, $500\,^{\circ}$ C, and $600\,^{\circ}$ C in air. A displacement-control mode was used, and an extensometer was utilized to record the displacement changes. Moreover, a data-acquisition rate of $100\,\text{Hz}$ was used. High-energy synchrotron x-ray diffraction (XRD) was performed at the Advanced Photon Source (APS), using the 11-ID-C beam-line located at the Argonne National Laboratory to obtain diffraction patterns of the deformed sample for structural characterizations, using a beam energy of $115.27\,\text{keV}$.

3. Modeling and analysis

3.1. Refined composite multiscale entropy modeling and analysis

In the past, entropy-based complexity measurements have been used to analyze the serrated flow in the low carbon steel, Al-Mg alloy, and HT-9 steel (Sarkar et al., 2007, 2010, 2015). The magnitude of the complexity of a time series is typically denoted as the sample entropy in which a higher value is typically characteristic of a less predictable behavior and more complex dynamical

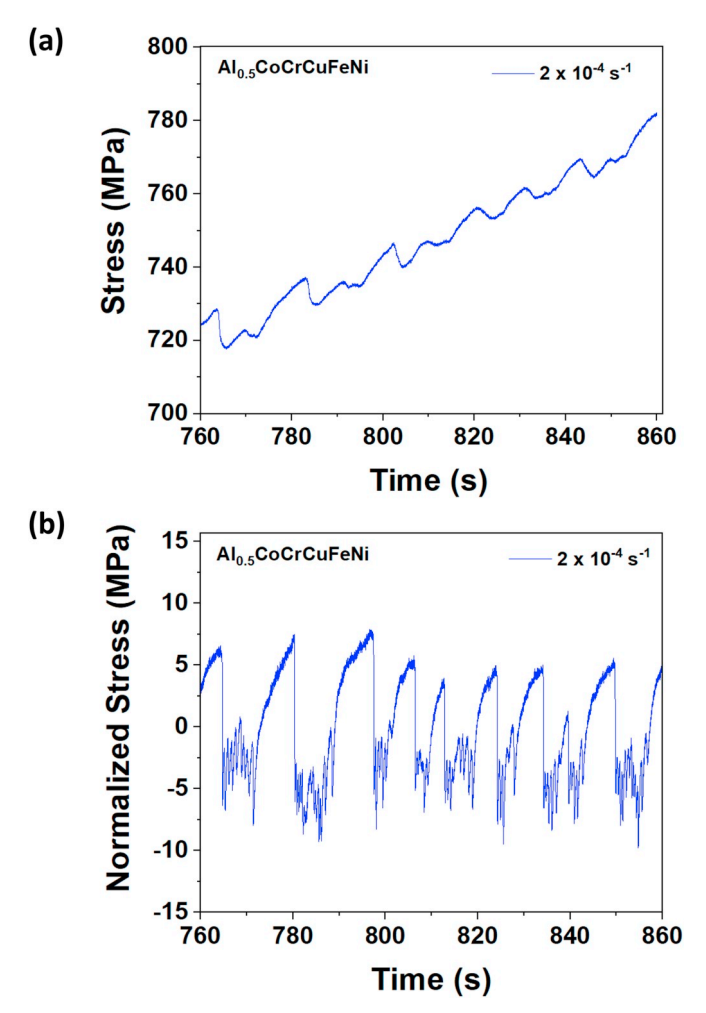


Fig. 2. Graphs for (a) stress vs. time series of the $Al_{0.5}$ CoCrCuFeNi HEA compressed at a strain rate of $2 \times 10^{-4} \, s^{-1}$ at a temperature of 500 °C and (b) corresponding detrended time series. (For the interpretation of the references to color in this figure legend, the reader is referred to the Web version of this article.)

behavior during the serrated flow. The results of these investigations found that the complexity of the serrations can be affected by the types of solute atoms present or deformation-band dynamics. For instance, Sarkar et al. found that a higher variety of interactions occurring in the carbon steel lead to the exhibited higher complexity values, as compared to the Al-Mg alloy. Here, substitutional atoms primarily act with only edge dislocations in the Al-Mg alloy, whereas in the steel, the interstitial solute atoms interact with both screw and edge dislocations (Sarkar et al., 2007).

To prepare data for the entropy modeling and analysis, one first eliminates the trend that arises in the work (strain) hardening regime (Sarkar et al., 2015). Here the stress vs. time data is fitted, using a third order polynomial in which the fit is subtracted from the original data (Iliopoulos et al., 2015). Fig. 2(a) and (b) show the time-series data for the sample compressed at 2×10^{-4} s⁻¹ and its detrended counterpart. With the processed time series, one constructs the coarse-grained time series, $y_{k,j}^{\tau}$, using the following equation (Wu et al., 2014):

$$y_{k,j}^{\tau} = \frac{1}{\tau} \sum_{i=(j-1)\tau+k}^{j\tau+k-1} x_i \; ; \; 1 \leq j \leq \frac{N}{\tau} \; ; \; 1 \leq k \leq \tau$$
 (1)

where x_i is the ith point from the original time-series data, X, k is an indexing factor, which tells us at which data point in the series to begin the modeling and analysis, N is the total number of data points from the original time series, and τ is the scale factor. One should notice that for k, $\tau = 1$ indicates that one recovers the original time series. Fig. 3(a)-(d) present the schematic for the coarse-grained series with k = 1–2 and $\tau = 2$ –3. Once $y_{k,j}^{\tau}$ is constructed, the next step is to write the time series of y_k^{τ} as a vector for each scale factor, τ (Wu et al., 2014):

$$y_{k}^{\tau} = \{ y_{k,1}^{\tau} y_{k,2}^{\tau} \dots y_{k,M}^{\tau} \}$$
 (2)

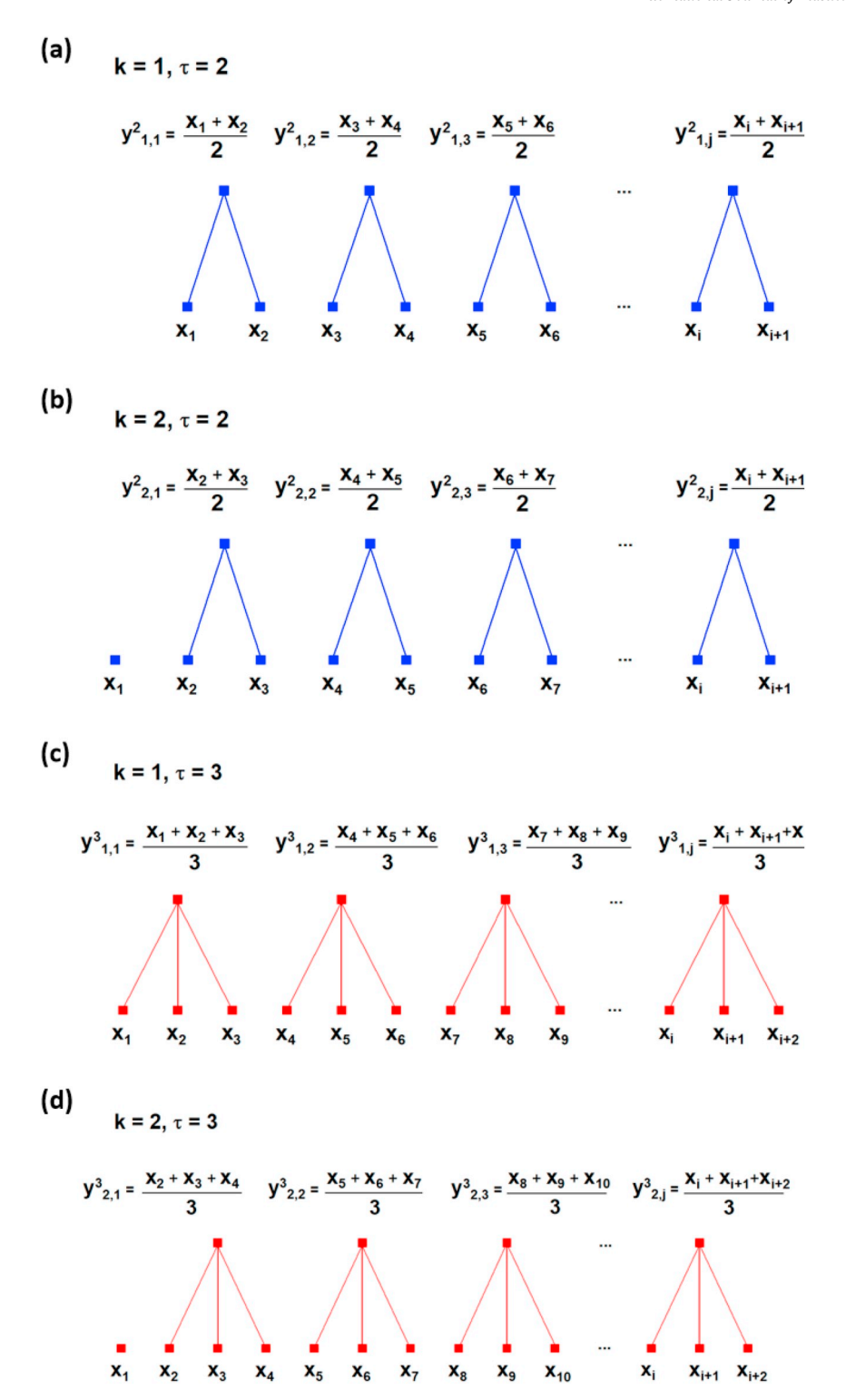


Fig. 3. Schematic for the coarse-graining procedure of (a) k = 1, $\tau = 2$, (b) k = 1, $\tau = 3$, (c) k = 2, $\tau = 2$, and (d) k = 2, $\tau = 3$. (For the interpretation of the references to color in this figure legend, the reader is referred to the Web version of this article.)

where $M = N/\tau$, and each $y_{i,i}^{\tau}$ is determined via Eq. (1). From here, make the template vectors of a dimension, m, (typically m = 2):

$$y_{k,i}^{\tau,m} = \{ y_{k,i}^{\tau} \ y_{k,i+1}^{\tau} \dots y_{k,i+m-1}^{\tau} \} ; \quad 1 \le i \le N-m ; 1 \le k \le \tau$$
 (3)

The next step in the process is to find n-matching sets of distinct template vectors for a given value of k. For the present work, the total number of matching vector sets for a given k, τ , and m will be designated as $n_{k,\tau}^m$. For two vectors to match, the difference between them (as defined by the infinity norm) must be less than a predefined tolerance value, r. Here the infinity norm, $d_{jl}^{\tau,m}$, is written as (Brechtl et al., 2018):

$$d_{jl}^{\tau,m} = ||\mathbf{y}_{j}^{\tau,m} - \mathbf{y}_{l}^{\tau,m}||_{\infty} = \max\{\left|y_{l,j}^{\tau} - y_{l,l}^{\tau}\right| \dots \left|y_{l+m-1,j}^{\tau} - y_{l+m-1,l}^{\tau}\right|\} < r$$

$$\tag{4}$$

According to (Costa et al., 2002, 2005; Costa and Goldberger, 2015), r is chosen as 0.15 times of the standard deviation of the data. The above value imposes a normalization effect on the data such that the sample entropy does not depend on the variance of the data. The above process is, then, repeated for template vectors of size, m + 1, where m is defined as above. Once the number of matching vectors, $n_{k,\tau}^m$, is found for m and m + 1, one sums this quantity from k = 1 to τ . Taking the natural log of the ratio of these two sums yields the refined composite multiscale entropy (RCMSE) value for the original data series (Wu et al., 2014):

$$RCMSE(X, \tau, m, r) = Ln\left(\frac{\sum_{k=1}^{\tau} n_{k,\tau}^{m}}{\sum_{k=1}^{\tau} n_{k,\tau}^{m+1}}\right)$$
(5)

Here, the sample entropy is only undefined when $n_{k,\tau}^m$ or $n_{k,\tau}^{m+1}$ are zero for all k. In comparison, the composite multiscale entropy (CMSE) method can have the undefined entropy when any $n_{k,\tau}^m$ or $n_{k,\tau}^{m+1}$ are zero. The advantage of this aspect for the RCMSE technique was shown in (Wu et al., 2014), where the RCMSE and CMSE algorithms were applied to model and analyze the 1/f noise, where f is defined as the frequency of the generated noise, which is bounded between arbitrarily small and large values. Here it was found that the RCMSE technique had the zero probability of inducing the undefined entropy for scale factors ranging from 1 to 20, whereas the CMSE algorithm had the non-zero probability for $\tau > 1$. This mitigation of the undefined entropy, therefore, makes the RCMSE technique a superior method, as compared to the CMSE algorithm, when modeling and analyzing the data.

3.2. Multifractal modeling and analysis

The time-dependent behavior exhibited by non-linear dynamical phenomena, such as the serrated flow in material systems (Bharathi et al., 2001, 2002) or the spatial distribution of dissipative regions in turbulent flows (Chhabra and Jensen, 1989; Meneveau and Sreenivasan, 1987), can many times be characterized via fractal or multifractal measures. In the present context, the fractal dimension characterizes the magnitude of the irregularity of a spatial structure or process quantitatively (Glenny et al., 1991). However, unlike the fractal approach, which can only characterize global scaling properties, the multifractal formalism examines both the underlying fractal geometry and the distribution of the underlying physical properties on the fractal support (Lebyodkin and Estrin, 2005).

The multifractal modeling and analysis, in terms of its application to the serrated flow, has been discussed in several works (Bharathi et al., 2001; Lebedkina and Lebyodkin, 2008; Lebedkina et al., 2014; Lebyodkin and Estrin, 2005; Lebyodkin et al., 2009, 2012; Lebyodkin and Lebedkina, 2006, 2008). This type of modeling and analysis has been used to examine the interplay between the serration type and the corresponding multifractal spectra. Bharathi et al. found that a burst in multifractality has been associated with the transition from Types B to A serrations (Bharathi et al., 2001). In another study, the multifractal characteristics of the serrated flow in the Al-Mg alloy was affected by the phase composition of the material (Lebyodkin and Estrin, 2005).

As a first step, the effect of strain hardening is intently discarded to de-trend the signal. This process is accomplished by subtracting the polynomial fit of the data, as was done for the RCMSE method. Once the data has been detrended, the numerical derivative, $\beta \approx \left|\frac{d\sigma}{dt}\right|_{t=t_1}$, which represents the bursts in the plastic activity, is computed. Next the data set is divided into non-overlapping windows of size, $\Delta \tau$, where the size of the window varies as $(\Delta \tau)^{2j}$ for j=1,2,... (Lebyodkin and Lebedkina, 2006; Lebyodkin et al., 2009). For each window, the normalized amplitude (probability measure), $p_i(\Delta \tau)$, of the plastic bursts is calculated. This value is equal to the sum of the amplitudes in the ith window divided by the sum of the magnitudes of the stress bursts in the entire data set and is written as:

$$p_i(\Delta \tau) = \frac{\left(\sum_{j=1}^M \beta_j\right)_i}{\sum_{k=1}^P \beta_k}$$
(6)

For the purposes of the statistical accuracy, the process of computing p_i ($\Delta \tau$) was repeated 10 times where the algorithm was initialized at random locations in the data set. Another important quantity is the measure, $\mu_i(\Delta \tau, q)$, which is equal to:

$$\mu_i(\Delta \tau, q) = \frac{p_i^q(\Delta \tau)}{\sum_i p_i^q(\Delta \tau)} \tag{7}$$

where q is a real number. From μ_i , the local singularity strength, α , which is useful for describing the scaling behavior of the heterogeneous data sets, is determined. More specifically, α gives the scaling relationship between the interval size and the

probability measure via p_i ($\Delta \tau$) ~ $\Delta \tau^{\alpha}$ and is calculated from the definition below (Bharathi et al., 2001; Salat et al., 2017):

$$\alpha = \lim_{\Delta \tau \to 0} \frac{\sum_{i} \mu_{i}(\Delta \tau, q) Ln[p_{i}(\Delta \tau)]}{Ln(\Delta \tau)}$$
(8)

It should be noted that in practice, the limit above cannot be calculated, and instead a linear-regression analysis is used (Appleby, 1996). Defining the quantity, $f(\alpha)$, also known as the fractal dimension of the subset of intervals characterized by the singularity strength, gives a scaling relationship between the number of time intervals, $N(\Delta \tau)$, comprising the data set, and its corresponding size, $\Delta \tau$, i.e., $N(\Delta \tau, \alpha) \sim \Delta \tau^{f(\alpha)}$.

$$f(\alpha) = \lim_{\Delta \tau \to 0} \frac{\sum_{i} \mu_{i}(\Delta \tau, q) Ln \mu_{i}(\Delta \tau)}{Ln(\Delta \tau)}$$
(9)

Similar to above, the linear-regression analysis must be used to solve for f, which describes the fractal dimension of the subset of intervals characterized by the α exponent (Song et al., 2015). In general, the plot of $f(\alpha)$ and α is calculated for q ranging from -10 to 10 and generally has a parabolic shape, if the corresponding spectrum is multifractal. The multifractal range, which is defined as $\Delta = \alpha_{\text{max}} - \alpha_{\text{min}}$, measures the inhomogeneity of the scaling behavior in each data set. The previous research suggested that a spike in the multifractal range at a specific strain rate indicated a transition from one serration type to another (Bharathi et al., 2001; Lebyodkin et al., 2009).

In addition to Δ , the generalized fractal dimension, D(q), may be calculated, using the Legendre transform through the following equation (Appleby, 1996; Salat et al., 2017):

$$D(q) = \frac{f(\alpha) - q\alpha}{1 - q} \quad ; \quad q \neq 1$$
(10)

where q, α , and $f(\alpha)$ are as defined above.

3.3. Complementary cumulative distribution function modeling and analysis

The complementary cumulative distribution function (CCDF), defined as C(S, q) where q is some control parameter, such as the applied strain rate or test temperature, gives the probability of observing a stress-drop size greater than a magnitude, S. Importantly, this type of analysis is used by experimentalists and theorists to model the stress-drop behavior in multiple systems, including bulk metallic glasses (Antonaglia et al., 2014b) and high entropy alloys (HEAs) (Carroll et al., 2015; Shi et al., 2017a; Zhang et al., 2014, 2017).

Zhang et al. used this type of modeling to investigate the effect of temperature on the weak spot (dislocations) avalanche dynamics in HEAs (Zhang et al., 2017). In another study, the model was employed to predict how the various experimental parameters would affect the behavior of the different types of serrations (Carroll et al., 2015). For instance, the model was able to predict the evolution of the serrated stress-strain curves from Types-A to B to C with increasing temperature. Moreover, they were able to determine that increasing the strain rate would lead to a transition in the serration behavior from Types-C to B to A in the HEA.

Mathematically speaking, C(S, q) is simply the integral of the probability distribution function of the stress-drop behavior from S to infinity, and can be written as:

$$C(S, q) = \int_{S}^{\infty} D(S, q) dS$$
(11)

For the present work, the CCDF will be modeled and analyzed for the serrated flow of the Al-containing HEA with respect to the strain rates ranging from 5×10^{-5} s⁻¹ - 2×10^{-3} s⁻¹ and test temperatures ranging from 400 °C to 600 °C.

4. Results

Fig. 4(a)-(c) show the stress vs. strain data for the experiments in which similar results were posted in (Chen et al., 2015, 2018d). As can be seen in the figures, the serrated flow displayed different behavior, which depended on the test temperature and strain rate. For the samples studied at 600 °C, the stress-drop behavior was characterized by Type-C serrations. For the other temperatures, the serrated flow exhibited either Type-A or B serrations. Table 1 gives a summary of the applied strain rate, test temperature, and serration type for the experiments. Similar results to those discussed above were reported in (Chen et al., 2018d).

One can see in the same graphs that at 500 °C, the fluctuations transitioned from behaving in a characteristically-periodic to more erratic fashion, as the strain rate was increased. For the samples tested at 400 °C, the amplitude of the serrations decreased with an increase in the strain rate. For the specimens tested at a strain rate of 5×10^{-5} s⁻¹, the stress increases at an accelerated rate (concave up) for 400 °C and 500 °C, while it rises at a decelerating rate (concave down) for 600 °C. The trend at 600 °C was similarly observed at the higher strain rates. Furthermore, at this strain rate, the amplitude of the stress rise was the smallest at 600 °C, while it was the largest at 400 °C.

Fig. 5(a)-(c) show the synchrotron x-ray diffraction patterns of the $Al_{0.5}$ CoCrCuFeNi HEA after compression at a strain rate of 2×10^{-3} s⁻¹ and test temperatures ranging from 400 to 600 °C. For the samples compressed at 400–500 °C, they were composed of a simple monolithic face-centered-cubic (FCC) structure. The samples tested at 600 °C, on the other hand, were found to be composed

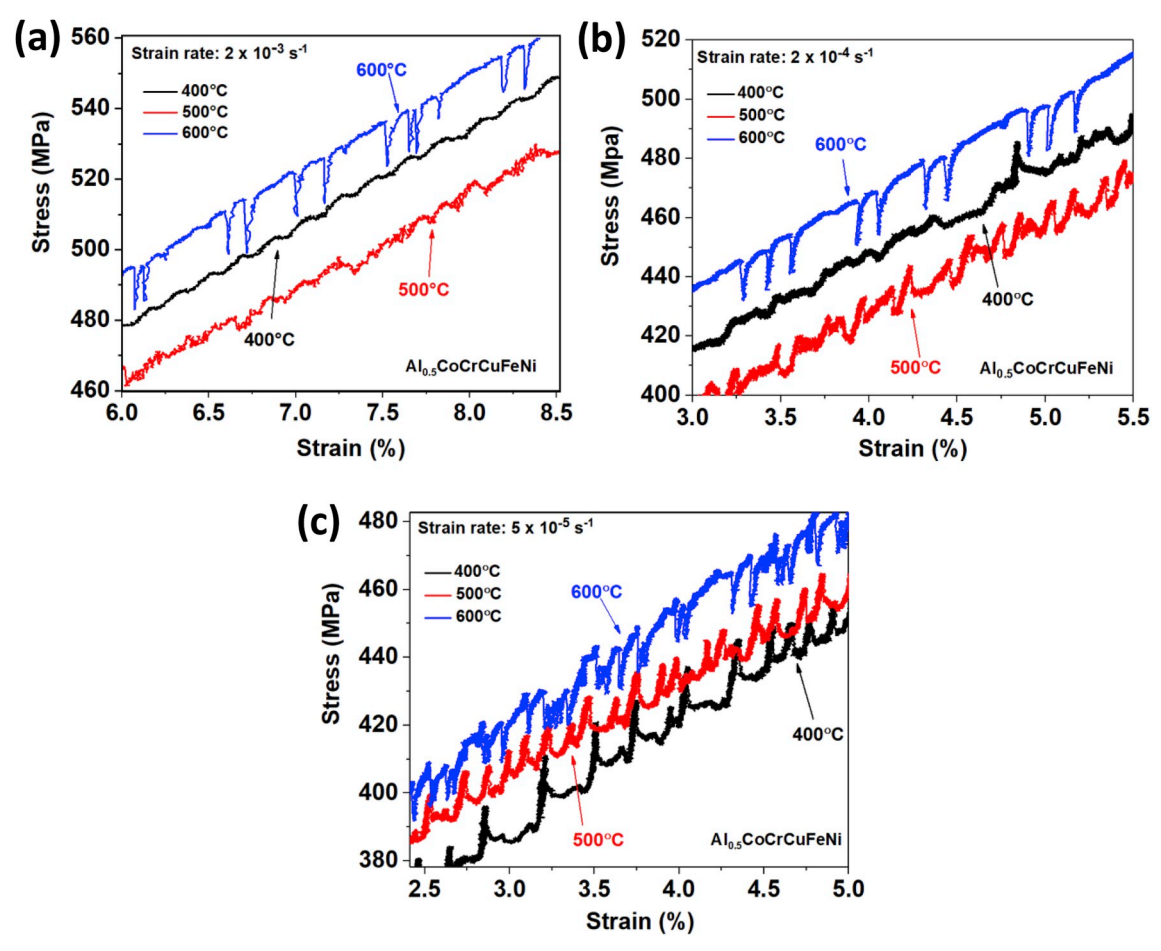


Fig. 4. Stress vs. strain graph for the Al_{0.5}CoCrCuFeNi HEA samples tested at strain rates of (a) 2×10^{-3} s⁻¹, (b) 2×10^{-4} s⁻¹, and (c) 5×10^{-5} s⁻¹ (Chen et al., 2015, 2018d). (For the interpretation of the references to color in this figure legend, the reader is referred to the Web version of this article.)

Table 1
Strain rates, test temperatures, and serration types for the experiments.

Strain Rate (s ⁻¹)	Temperature (°C)	Serration Type
2×10^{-3}	400	A
	500	Α
	600	С
2×10^{-4}	400	A
	500	В
	600	С
5×10^{-5}	400	A
	500	В
	600	С

of both the FCC and BCC structures. The RCMSE results of the experiments where the sample entropy was plotted for scale factors ranging from 1 to 20 are presented in Figs. 6(a)-(c). For the samples exposed to a strain rate of $5 \times 10^{-5} \, \mathrm{s}^{-1}$, the sample entropy (Sample En.) decreases for scale factors less than ~ 6 and then subsequently increases. However, this category of behavior becomes less apparent as the strain rate is increased. Moreover, the increase in the sample entropy with respect to strain rate becomes more pronounced for samples exposed at strain rates of $2 \times 10^{-4} \, \mathrm{s}^{-1}$ and $2 \times 10^{-3} \, \mathrm{s}^{-1}$ than at $5 \times 10^{-5} \, \mathrm{s}^{-1}$.

Furthermore, as can be seen in Fig. 6(a)-(c), the complexity, overall, was found to be higher for samples compressed at 500 °C and lower for those compressed at 600 °C, for all strain rates. It can also be surmised from the figure that the sample entropy increased

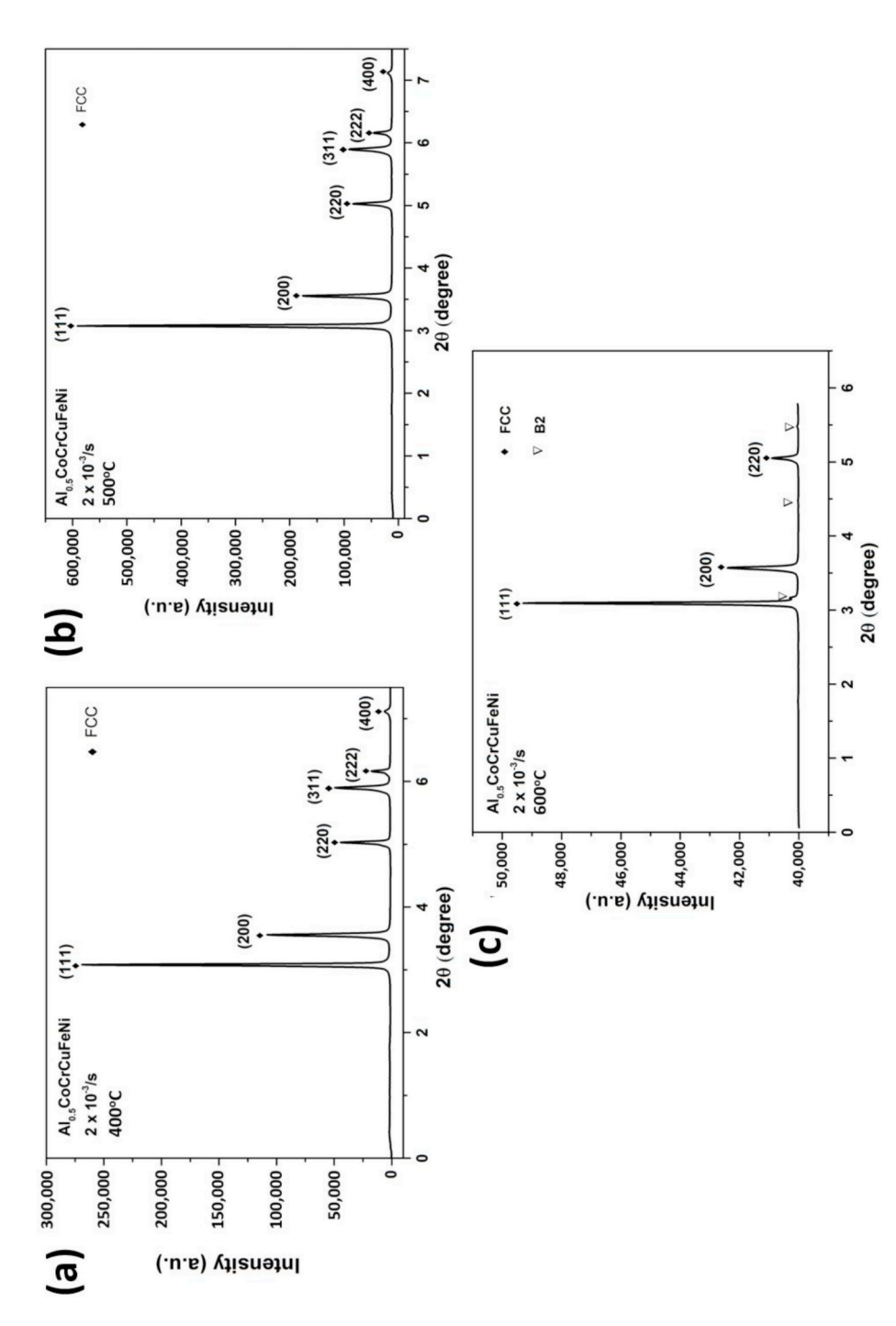


Fig. 5. X-ray diffraction patterns of the $Al_{0.5}$ CoCrCuFeNi HEA after compression at a strain rate of 2×10^{-3} s⁻¹ and test temperatures of (a) 400° C, (b) 500° C, and (c) 600° C.

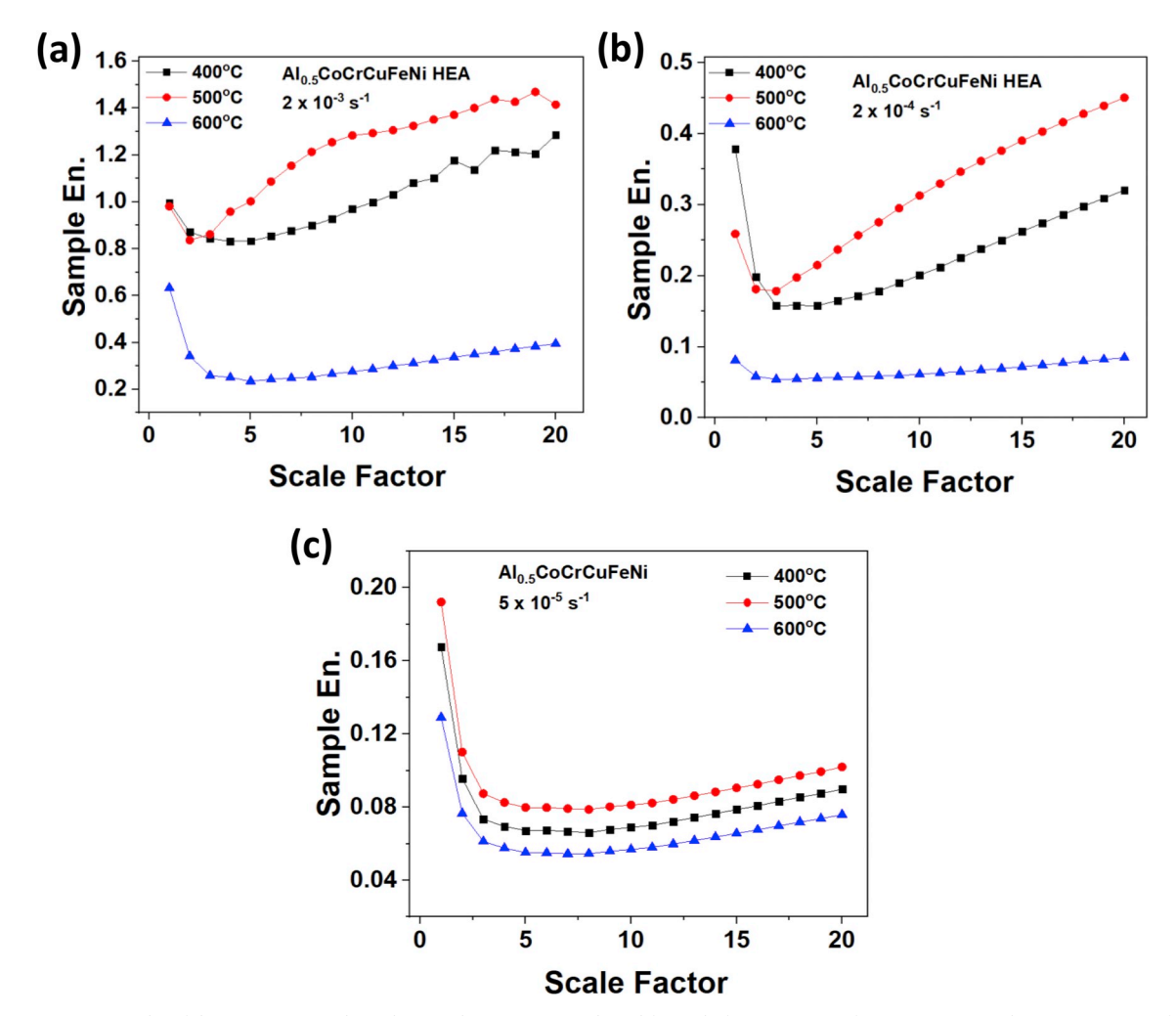


Fig. 6. RCMSE results of the experiments where the sample entropy was plotted for scale factors ranging from 1 to 20. (For the interpretation of the references to color in this figure legend, the reader is referred to the Web version of this article.)

dramatically with respect to strain rates at all test temperatures. Moreover, there was not much observable difference in the Sample En. curves for the specimens compressed at the lowest strain rate and different temperatures [see Fig. 6(c)]. Moreover, the complexity of the stress-drop behavior increases at larger scale factors under all strain rates and test temperatures. The above result indicates that the dynamics involved in the serrated flow contain complex structures and correlations across multiple scales.

Fig. 7(a)-(c) contain the plots of the histogram, Log [$D(\Delta\sigma)$], of the stress-burst magnitude, $\Delta\sigma$, for all experimental conditions. It can be observed from the graph that at a given temperature, the magnitude of the distributions decreased with increasing the strain rate. Furthermore, at a given strain rate, the samples tested at 600 °C generally experienced significantly higher stress bursts, ($\Delta\sigma$), as signified by larger values on the histograms. Furthermore, the spread of values was found to increase with respect to temperature under all strain rates. More specifically, the samples tested at 600 °C exhibited stress drops, which consisted of a higher number of extreme values. At strain rates of $2 \times 10^{-4} \, \text{s}^{-1}$ and $2 \times 10^{-3} \, \text{s}^{-1}$, the distributions [shown in Figs. 7(a)-(b)] for the samples tested at 500 °C contained a significant number of stress-burst values that were intermediate between the range of values for the histograms at other temperatures. The plots of the multifractal spectrum, $f(\alpha)$ vs. α , are presented in Fig. 8(a)-(c). The maximum value of the curves, which corresponds to the box-count dimension, D(0) [that can be seen in Fig. 9(a)-(c)], was found to be close to unity. The above result means that the geometrical support of the probability measure for the time-series data corresponds to a one-dimensional set (Lebyodkin and Estrin, 2005; Lebyodkin et al., 2009). At a given strain rate, the width of the spectrum was the largest for the samples undergoing compression at 600 °C. In general, the multifractality ($\Delta = \alpha_{\text{max}} - \alpha_{\text{min}}$) of the serrated flow appeared to increase with increasing temperature at a given strain rate. However, at a strain rate of $2 \times 10^{-3} \, \text{s}^{-1}$, the width of the spectrum did not change much from 400 °C to 500 °C, where the curves can be observed to be virtually on top of one another. In addition, the spread appeared to change less for the samples deformed at a strain rate of $5 \times 10^{-5} \, \text{s}^{-1}$. Finally, there was an une

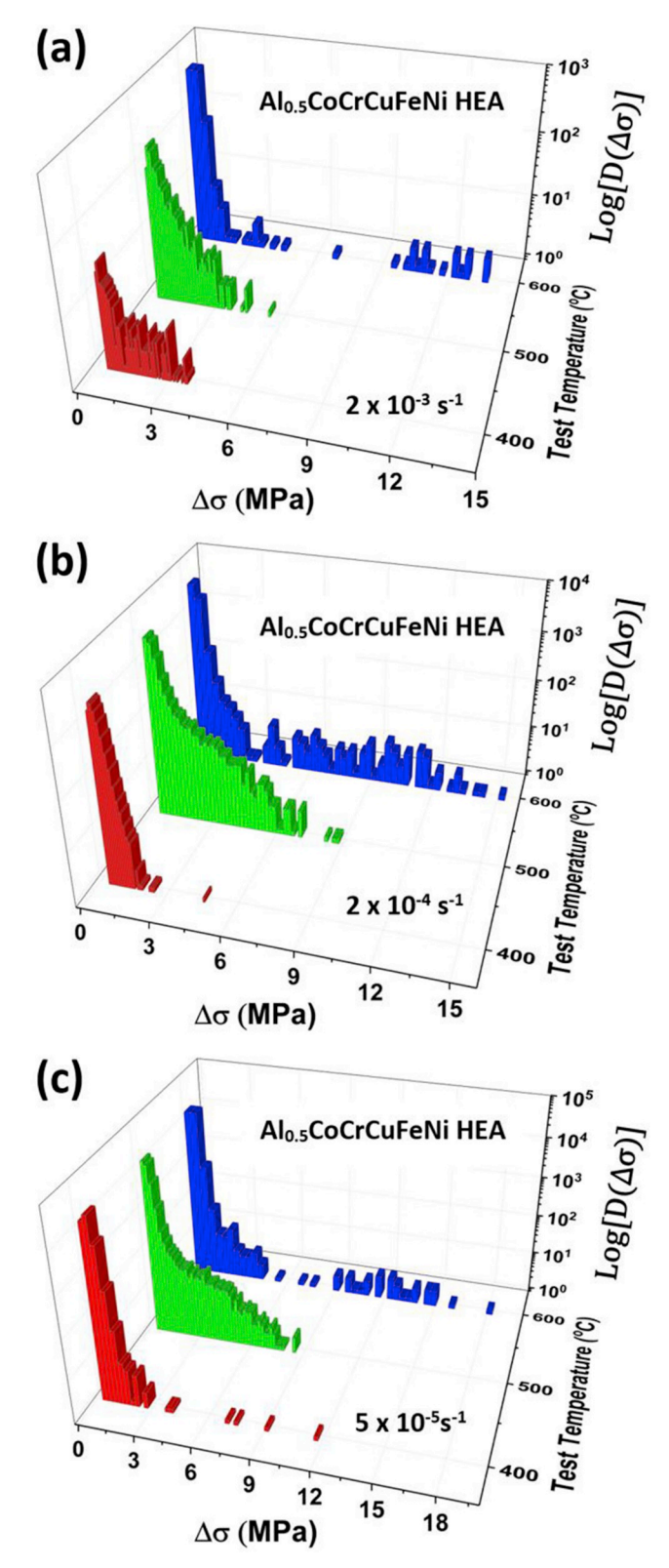


Fig. 7. Logarithmic distribution, Log [D ($\Delta\sigma$)], for the stress drop, $\Delta\sigma$, behavior of the Al_{0.5}CoCrCuFeNi HEA compression tested at strain rates of (a) 2×10^{-3} s⁻¹, (b) 2×10^{-4} s⁻¹, and (c) 5×10^{-5} s⁻¹, and test temperatures of 400 °C, 500 °C, and 600 °C, respectively. (For the interpretation of the references to color in this figure legend, the reader is referred to the Web version of this article.)

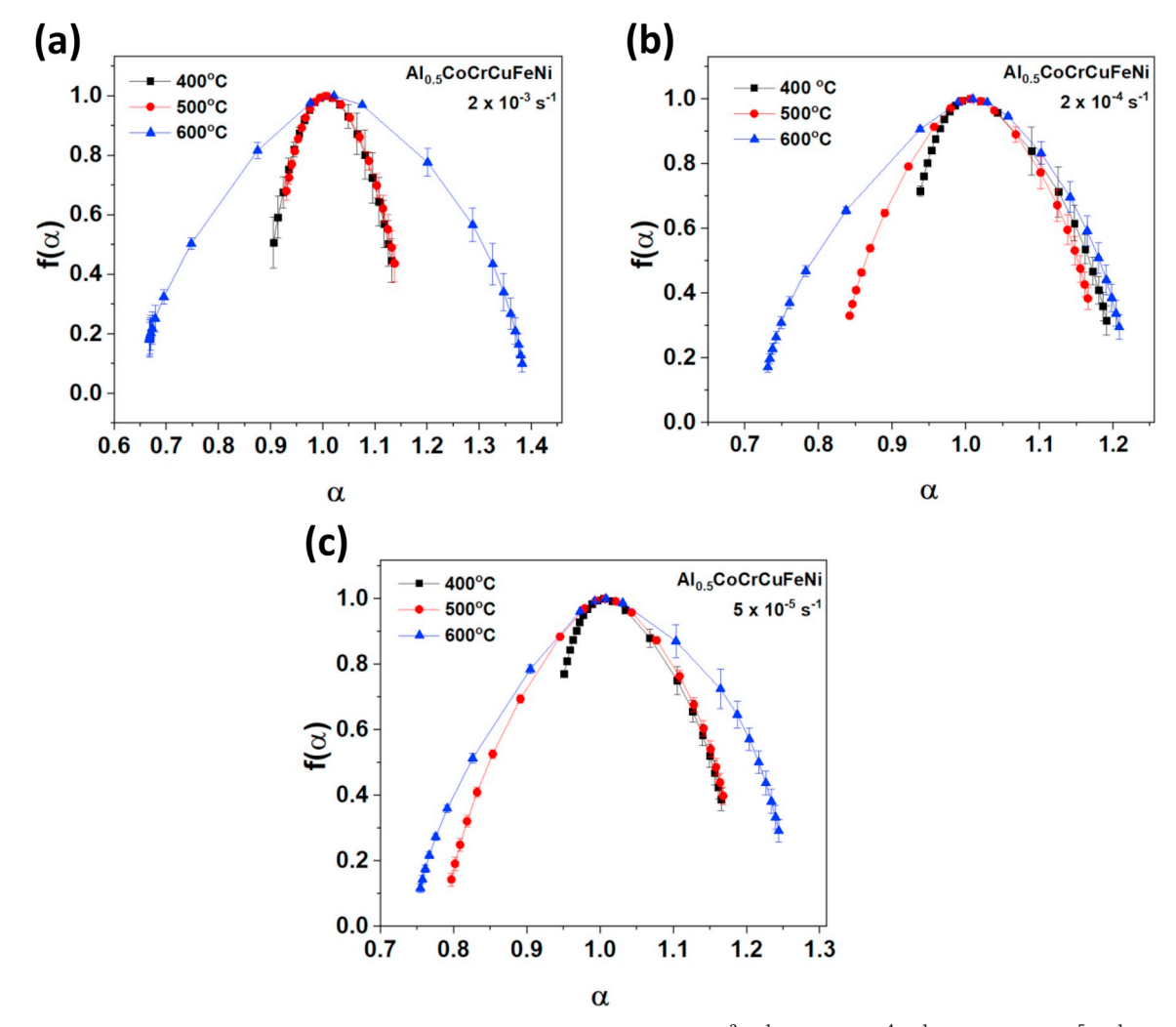


Fig. 8. Multifractal spectrum, $f(\alpha)$, vs. α for samples tested at strain rates of (a) 2×10^{-3} s⁻¹, (b) 2×10^{-4} s⁻¹, and (c) 5×10^{-5} s ⁻¹. (For the interpretation of the references to color in this figure legend, the reader is referred to the Web version of this article.)

q = 0 in Fig. 9(a)-(c), while there was no analogous feature for the corresponding multifractal spectra near the maximum f, as displayed in Fig. 8(a)-(c).

Fig. 10 shows the plot of the multifractality, Δ , vs. strain rate for each test temperature. Here, the multifractality was found to increase, overall, with increasing temperature at each strain rate. Additionally, there was a larger increase in Δ from 400 °C to 600 °C in the sample compressed at a strain rate of 2×10^{-3} s⁻¹, as compared to the other rates. Moreover, the samples tested at the other strain rates exhibited a similar increase in Δ with respect to temperature. Furthermore, at 600 °C, there was an observed burst in multifractality at a strain rate of 2×10^{-3} s⁻¹. With respect to the other strain rates, there was an overall increase in Δ with increasing temperature. The dimension on which the measure is distributed was on the generalized dimension, D(q), vs. q for $-20 \le q \le 20$ is plotted in Fig. 9(a)-(c). In general, the box-count dimension, D(0) (the fractal dimension on which the measure is distributed) was on the order of unity. Similar to Fig. 8(a)-(c), the curve is much wider for the data at 600 °C, as compared to other temperatures. This difference is especially noticeable for the samples compressed at a strain rate of 2×10^{-3} s⁻¹. In addition, the shift of the curve away from the unity for the samples tested at 500 °C (for q > 0) increases, as the strain rate is decreased. On the other hand, the samples compressed at 400 °C do not deviate far from unity for the positive q values.

Fig. 11(a)-(b) displays the CCDF of the stress drops that occur during serrations. The CCDF, in the context of the present work, gives the probability that at a given stress-drop value, there will be values, which are higher in magnitude. It was found that at a given strain rate, the CCDF curves shifted right as the test temperature increased. This behavior indicates that at a higher temperature, there will be a greater probability that a sample will experience a larger stress drop at a given strain rate. At a strain rate of $2 \times 10^{-3} \, \text{s}^{-1}$, there was a more pronounced difference in the curve at 600 °C, as compared to the curves at 400 °C and 500 °C. Furthermore, at a given strain rate, the samples tested at 600 °C exhibited the largest stress-drop values, as compared to the other temperatures.

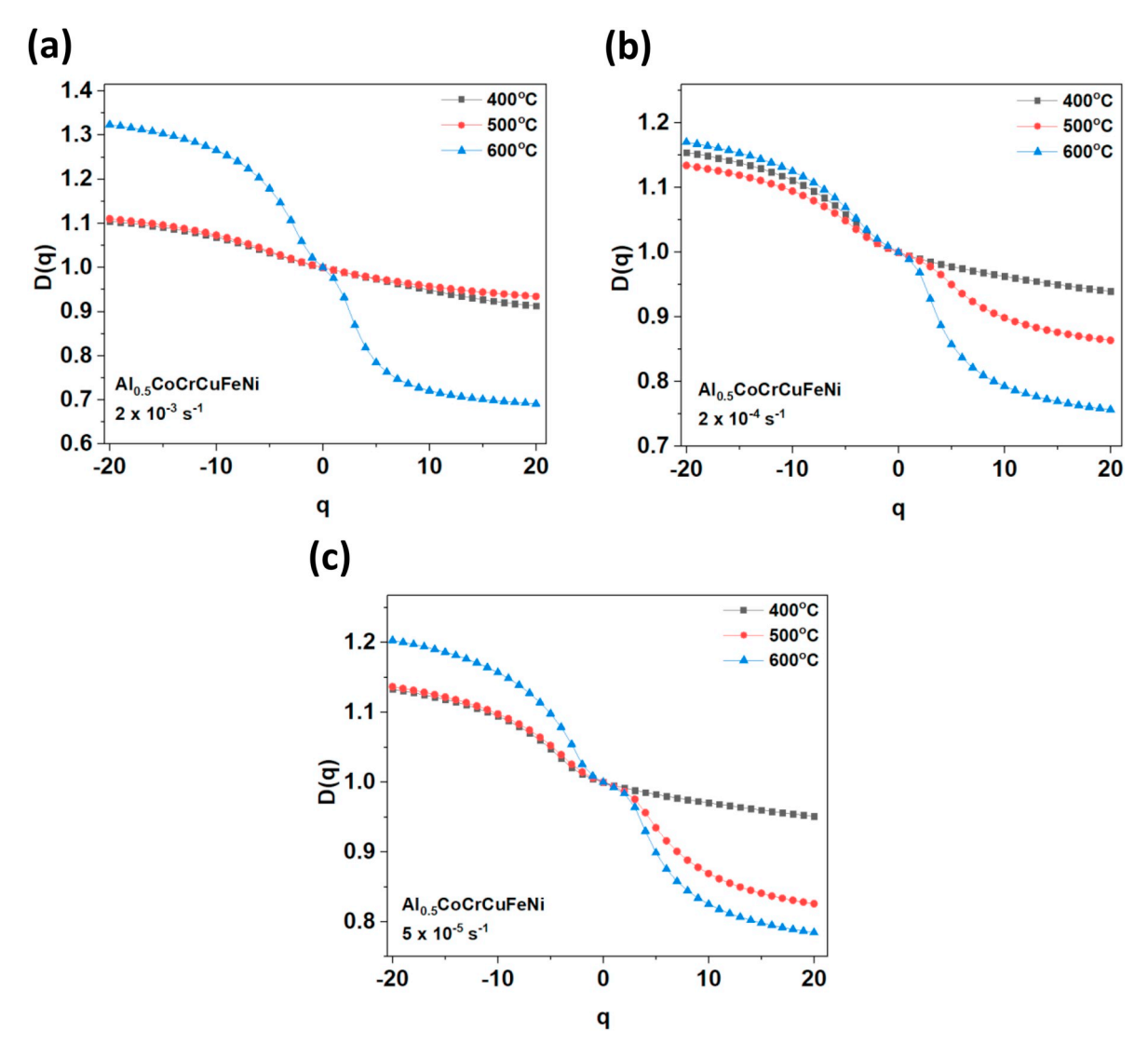


Fig. 9. Generalized dimension, D(q), vs. q for $-20 \le q \le 20$ for strain rates of (a) 2×10^{-3} s⁻¹, (b) 2×10^{-4} s⁻¹, and (c) 5×10^{-5} s⁻¹. (For interpretation of the references to color in this figure legend, the reader is referred to the Web version of this article.)

5. Discussion

5.1. Complexity modeling and analysis

The results of the complexity analysis, as presented in Fig. 6(a)-(c), show that the degree of long-range correlations in the serrated flow at 600 °C is significantly lower, as compared to 400 °C and 500 °C for a given strain rate. Therefore, the serrations at 600 °C can be thought to be more randomly-occurring events, as compared to the samples tested at 400 °C and 500 °C. From Table 1, it can be suggested that Types-A and B serrations are associated with more complex dynamical behavior, while Type-C serrations have a less intricate nature. A similar trend was reported in (Sarkar et al., 2010) where Type-B serrations, in general, exhibited the highest complexity, while Type-C displayed significantly-lower values (see Fig. 3 from the Reference). The higher complexity corresponds to the presence of deterministic chaos, which is inherent in the Type-B serrations (Sarkar et al., 2010). In the same figure [see Fig. 3 from (Sarkar et al., 2010)] Type-A serrations had the intermediate sample-entropy values for scale factors ranging from 4 to 19.

The serrated flow for the samples compressed at 500 °C appears to transition from behavior consisting of periodic oscillations to that, which has a less discernible pattern, as the strain rate is increased [see Fig. 4(a)-(c)]. A similar trend was observed at 400 °C for strain rates of 5×10^{-5} and 2×10^{-4} s⁻¹, although the behavior transitioned back into a periodic-like structure at 2×10^{-3} s⁻¹. Since the periodic behavior is typically less complex in nature (Costa et al., 2005, 2014), a transition from periodic to more erratic behavior should in theory lead to higher sample entropy values. This idea supports the results, as displayed in Fig. 6(a)-(c), where the sample-entropy at 400 °C and 500 °C increased significantly with increasing the strain rate. The larger sample-entropy values at

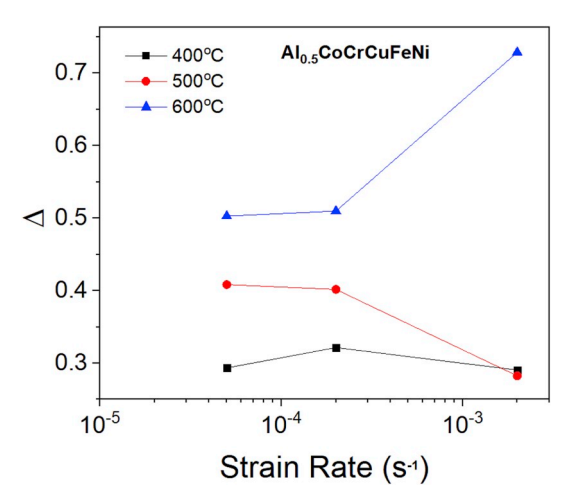


Fig. 10. Plot of Δ vs. strain rate for each test temperature. (For the interpretation of the references to color in this figure legend, the reader is referred to the Web version of this article.)

 $400\,^{\circ}\text{C}$ and $2\times10^{-3}\,\text{s}^{-1}$, as compared to the lower strain rates [see Fig. 6(a)-(c)], may be due to the presence of smaller, more dynamic fluctuations that accompany the more regular periodic oscillations.

As also observed in the same figures [see Fig. 6(a)-(c)], the sample entropy was found to generally increase with an increase in the strain rate. This rise in the complexity from the lowest to highest strain rates may be attributed to the decrease in the plastic-relaxation time, t_p , between successive drops. However, as t_p becomes comparatively smaller than the reloading time, new bands are allowed to form in the field of the unrelaxed internal stresses. Consequently, recurrent plastic events begin to overlap, which results in a hierarchy of length scales that is characteristic of more complex dynamics (Sarkar et al., 2010). In contrast, lower strain rates allow the material under compression to fully relax, leading to the reduced spatial correlation and, thus, simpler dynamics.

However, as can be seen in Fig. 6(a), the lower sample-entropy values, corresponding to 600 °C for the highest strain rate, appears to contradict the above assertion. Furthermore, the serrated flow exhibits similar behavior at this temperature for all strain rates, as observed in Fig. 4(a)-(c). The above results indicate that at higher temperatures, the strain rate has less of an influence on the complexity of the dynamical behavior of serrations during compression. Since the temperature is associated with the atomic mobility, it appears that at higher temperatures, diffusion has a greater influence on the serration dynamics, since it affects the ability of mobile atoms to pin and lock dislocations. Moreover, the increased mobility of atoms may lead to locking events that occur in a more rapid, less complex manner, as shown in Fig. 6(a)-(c).

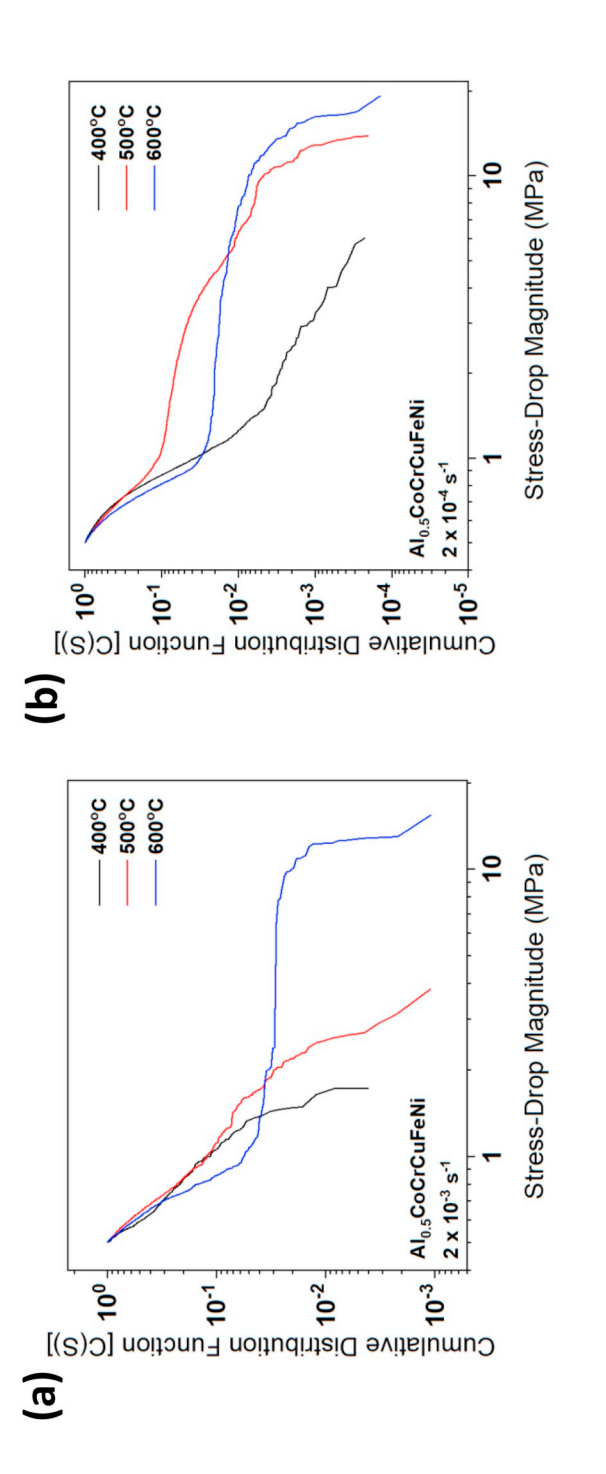
Following the results of Yasuda et al. (Niu et al., 2017; Yasuda et al., 2015), the effective pinning solute atoms are thought to be the Al atoms contained in the matrix, due to their atomic-size mismatch with the primary matrix atoms. More specifically, Al has the largest atomic radius of 1.43 Å, whereas the other elements have radii that range from 1.24 Å (Fe) to 1.28 Å (Cu). Here, a strain field will be produced around a solute by the atomic-size effect. Furthermore, a greater density of lattice sites with the localized strain will be caused by a higher concentration of substitutional solutes. Thus, in the multi-principal components alloys, more atomic-size differences in the lattice could be found to lead to large compressive and tensile strains surrounding a moving dislocation.

Furthermore, due to the size mismatch, the larger Al atoms will tend to segregate to the lower part in or near the core of the edge dislocations. It should also be mentioned that the mobile solutes always tend to diffuse to dislocations, where they form atmospheres that lower the overall energy (Bilby, 1950). As suggested by Niu (Niu et al., 2017), during an applied stress the Al-containing solute atmospheres will form around a moving dislocation core (Yoshinaga and Morozumi, 1971) or stacking fault (Hideji et al., 1952), which results in the DSA during plastic deformation.

The effect of mobility on the intricacy of locking dynamics may also be explained by the following discussion. For a strain rate of 5×10^{-5} s⁻¹, Chen et al. theorized that at 600 °C, the stress increase and subsequent drop were associated with locking events that involved a two-stage process (Chen et al., 2015). In contrast, a three-stage process was thought to occur at 400 °C and 500 °C. These two and three-stage processes are displayed in Fig. 12(a)-(b). As can be observed, the two-stage process is signified by an immediate, sharp increase in the stress after the stress-drop event while the three-stage process is signified as a gradual increase in the stress after the same event.

During the second stage of the latter process [see Fig. 12(b)], a variety of different types of interactions are thought to occur, such as the solute atom-dislocation line, dislocation line, dislocation line-precipitate interactions, and solute atom-solute atom interactions. With regards to the dislocation-dislocation interactions, it is hypothesized that this type of behavior is highly correlated in which the dislocations move in groups to form slip bands. At certain instances, the moving dislocations can pile-up against stable dislocation configurations (Miguel et al., 2001; Shetty, 2013). Importantly, stress fluctuations arising from these types of interactions are characterized by power-law statistics (Weiss et al., 2001; Yilmaz, 2011).

During the third stage [see Fig. 12(b)], the strain reaches a critical value in which the vacancy concentration is sufficient enough to activate solute atoms moving fast enough to pin the dislocation (Chen et al., 2015). Moreover, there may be interactions between



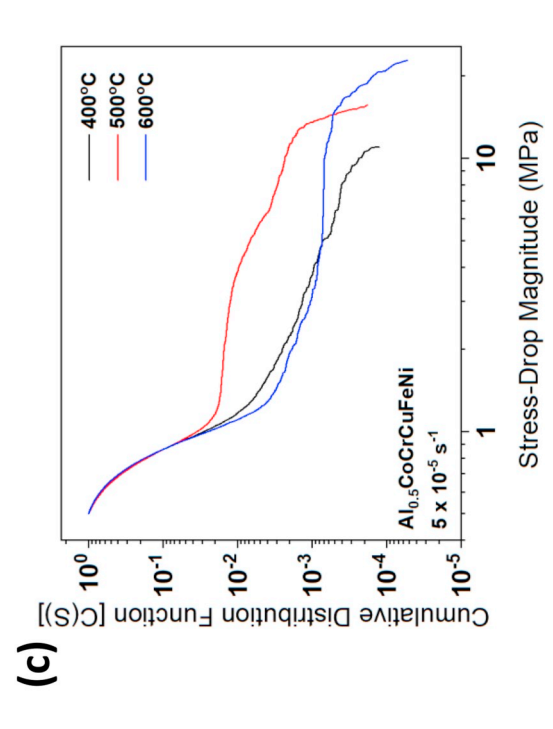


Fig. 11. Complementary cumulative distribution function (CCDF) (also known as survival functions) of the stress drops that occur during serrations for strain rates of (a) $2 \times 10^{-3} \, s^{-1}$, (b) $2 \times 10^{-4} \, s^{-1}$, and (c) $5 \times 10^{-5} \, s^{-1}$. (For the interpretation of the references to color in this figure legend, the reader is referred to the Web version of this article.)

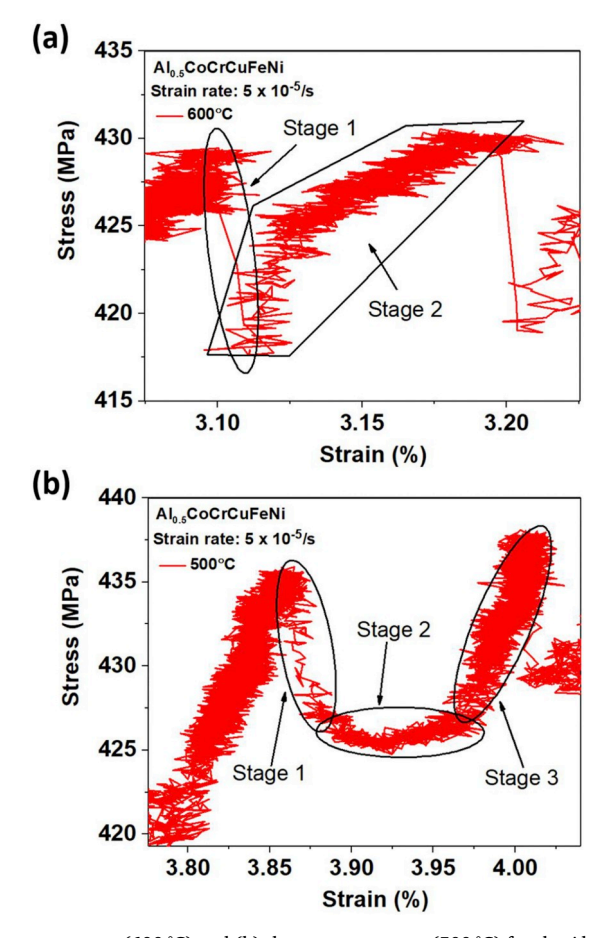


Fig. 12. Graphs featuring the (a) two-stage process (600 °C) and (b) three-stage process (500 °C) for the $Al_{0.5}$ CoCrCuFeNi HEA mechanically tested at a strain rate of 5×10^{-5} s⁻¹. Similar results were shown in (Chen et al., 2015). (For the interpretation of the references to color in this figure legend, the reader is referred to the Web version of this article.)

the dislocation lines and the fully-ordered $L1_2$ nanoparticles contained in the matrix. Once this trapping of dislocations by the solute atoms begins, the stress quickly rises to its maximum value. Therefore, this combination of the power-law scaling behavior during the second stage and the variety of defect interactions during the third stage is characteristic of more complex behavior during the serrations, as seen in the results of the sample-entropy analysis [see Figs. 6(a)-(c)]. On a final note, it should be stated that the above effect is not observed at 400 °C for the higher strain rates.

In contrast to the three-stage process, the lower number of stages involved during the serrated flow at 600 °C, as seen in Fig. 12(a), is a consequence of the increased migration speed of the atoms during compression. Here the solute atoms are moving fast enough such that they can immediately pin the dislocations after they break free, leading to another stress build-up event. This process of repeated pinning and unpinning of dislocation lines at the above temperature, which is akin to a set of dominos falling in succession, is thought to be governed by the very simple behavior, as exhibited by the relatively-low sample entropy and large Δ values in Fig. 6(a)-(c) and 10 (Sarkar et al., 2015).

Thus, the serration behavior that occurs at 400 °C and 500 °C is thought to be more complex, since it involves a more varied set of interactions, relative to 600 °C. In addition to what was discussed above, these interactions could perhaps include the impermanent trapping of mobile atoms by slower moving dislocation lines or perhaps vacancy clusters. In addition, the diffusion atoms may interact with other types of plastic instabilities. Moreover, this sophistication of the serrated flow at 500 °C is further increased at higher strain rates due to the overlapping of deformation bands, which leads to the interaction between the recurrent plastic events (Sarkar et al., 2010).

It should also be stated that previous testing conducted at temperatures beyond 600 °C yielded no serrated flows (Chen et al., 2015). The above text cited a couple of reasons for the disappearance of serrations. The reason for the decrease in the number of stress-drop events arises from the ability of dislocations to easily detach from the migrating solutes or from the ability of the solute to continuously move with the gliding dislocation during deformation.

In terms of microstructures, the results of the synchrotron XRD [see Fig. 5(a)-(c)], the structure of the HEA retained a full FCC structure during compression at 400 $^{\circ}$ C and 500 $^{\circ}$ C, whereas it transformed into a mixture of the FCC and B2 phases during testing at 600 $^{\circ}$ C. Furthermore, the TEM analysis revealed that partially-ordered L1₂ nano-particles were present in the material after testing at

500 °C, whereas fully-ordered $L1_2$ nano-particles resided in the matrix after testing at 600 °C (Chen et al., 2018b). As discussed by Diao et al., FCC-structured HEAs are typically more ductile, while BCC-structured HEAs exhibit higher strengths but lower plasticity (Diao et al., 2017). The above results, therefore, suggest a few things. Firstly, the increase in the complexity of the serrated flow, as observed in Fig. 6(a)-(c) for the samples tested at 500 °C, may be caused by the introduction of the partially-ordered $L1_2$ phases. Secondly, the significant drop in the complexity, as seen in the samples compressed at 600 °C, appears to be linked to the presence of the fully-ordered $L1_2$ phase in addition to a decrease in the ductility caused by the introduction of the BCC phase into the matrix.

5.2. Multifractal modeling and analysis

Interestingly, as shown in Fig. 8(b)-(c), the width of the multifractal spectra increased with increasing the test temperature, which suggests that the temperature played a role in the homogeneity of the serrated flow in the alloys during compression. For the sample tested at a strain rate of 2×10^{-3} s⁻¹ [see Fig. 8(a)], this difference was not significant for temperatures of 400 °C and 500 °C, although the spread was significantly larger at 600 °C. The above result suggests that unlike the lower strain rates, a change from 400 °C to 500 °C did not affect the degree of the heterogeneity in the serrated flow. As can be seen in Fig. 4(a)-(c), it appears that larger multifractal spectra are associated with Type-C serrations, which occurred at 600 °C. On the other hand, smaller spectra are found to be associated with Types-A and B serrations that occurred at 400 °C and 500 °C. It should also be mentioned that the point of inflection, as observed in Fig. 9(a)-(c) around q = 0, may be ascribable to the statistical error in the data or a fundamental limitation of the algorithm (PastorSatorras and Riedi, 1996). The fact that there was no similar discrepancy in the multifractal spectra, as displayed in Fig. 8(a)-(c), further supports this idea.

This effect of temperature on the multifractality is more apparent in Fig. 10, where the heterogeneity of deformation was found, in general, to increase with increasing test temperature, as evidenced by an increase in multifractality. In the above context, an increase in the multifractal spectra is indicative of more heterogeneous deformation mechanisms. This trend can be seen in Fig. 10, where Δ was noticeably higher for the samples compressed at 600 °C, as compared to the other temperatures. It should also be mentioned that an increasing trend similar to the one at 600 °C was also observed in the polycrystalline Al-Mg when exposed to similar strain rates at room temperature (Bharathi et al., 2002; Lebyodkin et al., 2009). However, the multifractality of the serrated flow in the same alloy decreased at strain rates above 1.4×10^{-3} s⁻¹ during the same experiment. From this result, it is speculated whether a similar drop in Δ will occur in the multifractal spectra of the Al_{0.5}CoCrCuFeNi HEA compressed at strain rates above 2×10^{-3} s⁻¹ and 600 °C (see Fig. 10). It should also be mentioned that at 600 °C, the studied alloy demonstrates an opposite effect of the strain rate on the shape of the serrations, as compared with the Al-Mg alloy (Bharathi et al., 2001). It may also be thought that in contrast to binary alloys, the best similarity with the Type-C effect on the multifractal spectra is found at the highest strain rate of 2×10^{-3} s⁻¹.

In contrast to the increase in the multifractality at 600 °C, Δ , overall, decreased with increasing strain rates at 400 °C and 500 °C. The decreasing trend in Δ indicates that the homogeneity of the serrated flow increased at lower temperatures and higher strain rates. This decrease in the multifractality indicates that the scale hierarchy of the serrated flow in the Al_{0.5}CoCrCuFeNi HEA may correspond to the self-organized criticality in the above conditions (Bharathi et al., 2002; Lebyodkin et al., 2009). The above statement is supported by the observation that Type-A serrations (400 °C and 500 °C), which are signified by the self-organized critical behavior (Sarkar et al., 2010), were found to correspond to smaller spectra [see Fig. 8(a)-(c) and 10] in the present work.

As discussed in (Lebyodkin et al., 2012; Lebyodkin and Lebedkina, 2008), a rise in the multifractality of the serrated flow at 600 °C may be due to a decrease in the number of mobile dislocations participating in the correlated process, in addition to, uncorrelated events happening concomitantly. Moreover, the emergence of the fully-ordered L1₂ nano-particles and the B2 phase at the above temperature appears to be linked to the increased multifractality [see Fig. 8(a)-(c) and 10] of the serrated flow. Perhaps the BCC phase leads to the efficient homogenization of plastic incompatibilities, and, consequently, to weakly-correlated bands that nucleate in a random fashion, which is exhibited by an increase in Δ (Lebedkina and Lebyodkin, 2008). Furthermore, the increase in the multifractality at 600 °C in Fig. 10 appears to correspond to an increase in the Young's modulus at that temperature as well (Chen et al., 2015).

5.3. Statistical analysis

From the histogram and CCDF analysis of the stress-drop behavior, as seen in Fig. 7(a)-(c) and 11, it is apparent that the serrations that occurred at 600 °C are accompanied by the largest S_{max} values, as compared to the samples tested at other temperatures. The samples deformed at 600 °C exhibited a larger tail in the CCDF curves, which appears to be associated with a decrease in the complexity and increase in the multifractality of the serrated flow, as exhibited in Fig. 6(a)-(c) and 10. The larger tail corresponds to the Type-C serrations [as observed in Fig. 4(a)-(c)], which typically has a larger proportion of stress drops that are greater in magnitude, as compared to other serration types. Moreover, the larger stress drops associated with these types of serrations appears to be linked to the emergence of the $L1_2$ nano-particles and the B2 phase in the matrix that may be accompanied by a decrease in the plasticity of the alloy.

In contrast, serrations that had a lower probability of having larger stress drops, as exhibited in Type-A and B serrations at 400 °C and 500 °C, [see Fig. 11(a)-(c)], tended to behave in a more complex manner [Fig. 6(a)-(c)]. Moreover, these types of serrations also consisted of stress bursts that exhibited a lower spread in the multifractal spectra [Fig. 8(a)-(c) and 11(a)-(c)]. Interestingly, the most complex serrations, which occurred at 500 °C, were associated with S_{max} values that were intermediate between the samples tested at the other temperatures. These intermediate stress-drop values at this temperature appear to correspond to the intermediate uniformity in the stress-burst behavior, as can be observed in Fig. 8(a)-(c) and 11(a)-(c). The above result suggests that a higher degree of

meaningful structural richness in the serrated flow corresponds to stress drops that possess intermediate values and in which the dynamical behavior is somewhat uniform.

5.4. Towards a greater understanding

As previously discussed, the irregularity or the serial randomness of the serration behavior was the highest for samples tested at 500 °C [as observed in Fig. 6(a)-(c)], which was accompanied, in general, by the intermediate Δ values, as shown in Fig. 10. Moreover, the multifractality was the smallest for the samples compressed at 400 °C for strain rates less than 2×10^{-3} s $^{-1}$, as presented in the same graph. Here, the multifractality describes the degree of heterogeneity in the underlying serrated flow. The decreased inhomogeneity in the stress-drop behavior at this temperature may arise from a lower number of dislocation line/solute atom interactions due to a noticeably-slower migration speed of the diffusing Al atoms during testing. It is thought that the dynamical complexity of the three-stage process at the above temperature is easily modified by a slight change in the degree of heterogeneity of the stress-burst behavior. In contrast, the irregularity of the serrated flow is much less affected by a change in the heterogeneity of the stress bursts. From here, it can be theorized that the underlying two-stage process driving the serrated flow at 600 °C retains its simplistic behavior despite an increase in the randomness of the stress-burst dynamics with an increase in the strain rate [see Fig.6(a)-(c)].

As can be seen in Fig. 6(a)-(c), the samples tested at 500 °C exhibited the highest spatiotemporal correlations in the serrated flow. In addition, they had a larger portion of serrations that consisted of stress-drops values that ranged between those associated with the other test temperatures, as observed in Fig. 7(a)-(c). This range of values in the magnitude at the above temperature appears to be associated with serrations, which have more complex structures (as discussed in the previous section) across all spatiotemporal scales.

As discussed earlier, the three-stage process, which occurs at $500\,^{\circ}$ C, involves more intricate dynamics underlying the serrated flow. It appears that this more structurally-rich behavior corresponds to locking events that are associated with stress bursts, which are more heterogenous, as compared to $400\,^{\circ}$ C. Specifically, these more complex dynamics appear to lead to greater stress drops after the dislocations break free of the mobile atoms. From the above, it may be thought that as the temperature increases from $400\,^{\circ}$ C to $500\,^{\circ}$ C, the higher atom mobility affects the pinning effectiveness and, therefore, the conditions for the collective motion of dislocations. This change in the collective behavior of the dislocations, which is altered by the solute-pinning effectiveness, leads to a more complicated locking structure that alters the size and shape of the serrations. However, once the temperature approaches $600\,^{\circ}$ C, the interactions become more random in nature, due mainly to the increased rate at which dislocations are pinned by the mobile solute atoms. This increased rate of interactions may be due to the increased time that the dislocations are trapped due to the fully-ordered L1₂ nano-particles. Moreover, this higher degree of randomness during the serrated flow corresponds to an even greater level of heterogeneity of the corresponding stress-burst values, which suggests that there is an optimal level of heterogeneity in which the complexity goes from being positively correlated with the multifractality to being negatively correlated.

Finally, as discussed earlier, there appears to be an interesting link among the complexity, multifractal spectra, the stress-drop magnitude, and the types of phases present in the material. For the samples tested at 600 °C, the existence of the fully-ordered L1₂ nano-particles and B2 phase in the matrix during compression leads to serrations that are characterized by the Type-C behavior, low complexity, wide multifractal spectra, and larger stress drops. Furthermore, the results of previous experiments suggest that the above trend may be associated with a drop in the plasticity due to the presence of the B2 phase. In contrast, serrations that were characterized by a higher level of complexity and narrower multifractal spectra [see Fig. 6(a)-(c) and Fig. 8(a)-(c)] were associated with only the partially-ordered L1₂ nanoparticles contained in the material during the test. However, the effects of the nanoparticles on the complexity of the serrated flow are not well understood, and will hopefully be the subject of future investigations.

6. Conclusions

The serrated flow was investigated in the $Al_{0.5}$ CoCrCuFeNi HEA undergoing compression testing at strain rates ranging from 5×10^{-5} - 2×10^{-3} s $^{-1}$ and temperatures varying from 400 °C to 600 °C. Based on the results of the experiments, many conclusions were obtained. In terms of the complexity of serrations, they were reported to increase significantly with increasing the strain rate, where it was found to be, generally, the highest at 500 °C and the lowest at 600 °C for all strain rates [see Fig. 6(a)-(c)]. Moreover, the higher sample entropy observed at 500 °C was linked to the stress-drop behavior that had intermediate values in terms of S_{max} , Δ , and histogram distributions (see Figs. 8 and 10). The lower sample-entropy values at 600 °C were attributed to unpinning events, followed immediately by the pinning of dislocation lines through migrating solute atoms.

In contrast, the enhanced irregularity in the serrations at $500\,^{\circ}$ C appears to be linked to the three-step process in which there is a greater degree of intricacy associated with the pinning and unpinning of dislocations. Furthermore, the strain rate appeared to have a larger influence, as compared to temperature, on the sample entropy of the serrated flow. The multifractality of the serration behavior was found to be the largest for the samples tested at $600\,^{\circ}$ C, and the lowest for $400\,^{\circ}$ C, at a given strain rate. In terms of the serration types, Type-C serrations were associated with the lowest complexity values, highest multifractal spectra, and greater probability of exhibiting larger stress drops. Conversely, Type-A and B serrations were associated with the higher complexity, smaller spectra, and lower probability of higher stress drops.

Lastly, the incorporation of the fully-ordered $L1_2$ nano-particles and BCC phase structure in the alloy during testing at 600 °C may be linked to a lower degree in the spatiotemporal correlations of the serrations in the alloy, in addition to a decrease in the ductility of the alloy. Conversely, the presence of partially-ordered $L1_2$ nano-particles, as observed in the samples that underwent compression at

500 °C, corresponded to a higher degree of complexity in the serrated flow. However, further work will be needed to verify these assessments.

Funding and Acknowledgements

P. K. L., S. Y. C., and X. X. are grateful for the support of the National Science Foundation (DMR-1611180 and 1809640), and the Department of Energy (DOE) Office of Fossil Energy, National Energy Technology Laboratory (NETL) (DE-FE0008855, DE-FE-0024054, and DE-FE-0011194), with Drs. G. Shiflet, D. Farkas, V. Cedro, R. Dunt, S. Markovich, and J. Mullen as program managers. P.K.L. very much appreciates the support from the U.S. Army Office Project (W911NF-13-1-0438) with the program managers, Drs. M. P. Bakas, S. N. Mathaudhu, and D. M. Stepp. P. K. L. and S. Y. C. would like to acknowledge the financial support of the Center for Materials Processing (CMP), at the University of Tennessee, with the director of Dr. Claudia J. Rawn. The present research used resources of the Advanced Photon Source, a U.S. Department of Energy Office of Science User Facility operated for the DOE Office of Science by the Argonne National Laboratory under the Contract No. of DE-AC02-06CH11357. The authors would also like to thank Dr. K. A. Dahmen for helpful discussions regarding this manuscript.

Author contributions

All authors contributed extensively to the work presented in this manuscript. S. Y. C. and J. W. Q. performed the mechanical testing and sample preparation. J. B. and X. X. modeled and analyzed the serration data. S. Y. C. and Y. R. performed the X-ray diffraction experiments. J. B., S. Y. C., P. K. L., and S. J. Z. wrote the main manuscript. All authors discussed the results and implications and commented on the manuscript at all stages.

Declarations of interest

None.

Appendix A. Supplementary data

Supplementary data to this article can be found online at https://doi.org/10.1016/j.ijplas.2018.11.011.

References

- Antonaglia, J., Wright, W.J., Gu, X., Byer, R.R., Hufnagel, T.C., LeBlanc, M., Uhl, J.T., Dahmen, K.A., 2014a. Bulk metallic glasses deform via slip avalanches. Phys. Rev. Lett. 112, 1–5.
- Antonaglia, J., Xie, X., Schwarz, G., Wraith, M., Qiao, J., Zhang, Y., Liaw, P.K., Uhl, J.T., Dahmen, K.A., 2014b. Tuned critical avalanche scaling in bulk metallic glasses. Sci. Rep. 4, 4382.
- Appleby, S., 1996. Multifractal characterization of the distribution pattern of the human population. Geogr. Anal. 28, 147-160.
- Benallal, A., Berstad, T., Borvik, T., Hopperstad, O.S., Koutiri, I., de Codes, R.N., 2008. An experimental and numerical investigation of the behaviour of AA5083 aluminium alloy in presence of the Portevin-Le Chatelier effect. Int. J. Plast. 24, 1916–1945.
- Bharathi, M.S., Lebyodkin, M., Ananthakrishna, G., Fressengeas, C., Kubin, L.P., 2001. Multifractal burst in the spatiotemporal dynamics of jerky flow. Phys. Rev. Lett. 87 (4), 165508.
- Bharathi, M.S., Lebyodkin, M., Ananthakrishna, G., Fressengeas, C., Kubin, L.P., 2002. The hidden order behind jerky flow. Acta Mater. 50, 2813-2824.
- Bilby, B.A., 1950. On the interactions of dislocations and solute atoms. Proc. Phys. Soc. Lond. Section A 63, 191-200.
- Brechtl, J., Xie, X., Liaw, P.K., Zinkle, S.J., 2018. Complexity modeling and analysis of chaos and other fluctuating phenomena. Chaos, Solit. Fractals 116, 166–175. Cai, B., Liu, B., Kabra, S., Wang, Y., Yan, K., Lee, P.K., Liu, Y., 2017. Deformation mechanisms of Mo alloyed FeCoCrNi high entropy alloy: in situ neutron diffraction. Acta Mater. 127, 471–480.
- Cai, Y.L., Tian, C.G., Fu, S.H., Han, G.M., Cui, C.Y., Zhang, Q.C., 2015. Influence of gamma 'precipitates on Portevin-Le Chatelier effect of Ni-based superalloys. Mater. Sci. Eng. A-Struct. Mater. Prop. Microstruct. Process. 638, 314–321.
- Cantor, B., Chang, I.T.H., Knight, P., Vincent, A.J.B., 2004. Microstructural development in equiatomic multicomponent alloys. Mater. Sci. Eng. A-Struct. Mater. Prop. Microstruct. Process. 375, 213–218.
- Carroll, R., Lee, C., Tsai, C.-W., Yeh, J.-W., Antonaglia, J., Brinkman, B.A.W., LeBlanc, M., Xie, X., Chen, S., Liaw, P.K., Dahmen, K.A., 2015. Experiments and model for serration statistics in low-entropy, medium-entropy, and high-entropy alloys. Sci. Rep. 5, 16997.
- Chatterjee, A., Sarkar, A., Barat, P., Mukherjee, P., Gayathri, N., 2009. Character of the deformation bands in the (A + B) regime of the Portevin-Le Chatelier effect in Al-2.5%Mg alloy. Mater. Sci. Eng. 508, 156–160.
- Chen, P.Y., Lee, C., Wang, S.Y., Seifi, M., Lewandowski, J.J., Dahmen, K.A., Jia, H.L., Xie, X., Chen, B.L., Yeh, J.W., Tsai, C.W., Yuan, T., Liaw, P.K., 2018a. Fatigue behavior of high-entropy alloys: a review. Sci. China Technol. Sci. 61, 168–178.
- Chen, S., Li, W., Xie, X., Brechtl, J., Chen, B., Li, P., Zhao, G., Yang, F., Qiao, J., Liaw, P.K., 2018b. Nanoscale serration and creep characteristics of Al_{0.5}CoCrCuFeNi high-entropy alloys. J. Alloy. Comp. 752, 464–475.
- Chen, M., Shi, X.H., Yang, H., Liaw, P.K., Gao, M.C., Hawk, J.A., Qiao, J., 2018c. Wear Behavior of Al_{0.6}CoCrFeNi high-entropy alloys: effect of environments. J. Mater. Res. 33, 3310–3320.
- Chen, S., Xie, X., Chen, B.L., Qiao, J.W., Zhang, Y., Ren, Y., Dahmen, K.A., Liaw, P.K., 2015. Effects of temperature on serrated flows of Al_{0.5}CoCrCuFeNi high-entropy alloy. JOM 67, 2314–2320.
- Chen, S., Xie, X., Li, W., Feng, R., Chen, B., Qiao, J., Ren, Y., Zhang, Y., Dahmen, K.A., Liaw, P.K., 2018d. Temperature effects on the serrated behavior of an Al_{0.5}CoCrCuFeNi high-entropy alloy. Mater. Chem. Phys. 210, 20–28.
- Chen, S., Yu, L., Ren, J., Xie, X., Li, X., Xu, Y., Zhao, G., Li, P., Yang, F., Ren, Y., Liaw, P.K., 2016. Self-similar random process and chaotic behavior in serrated flow of high entropy alloys. Sci. Rep. 6, 29798.
- Chen, S.Y., Yang, X., Dahmen, K.A., Liaw, P.K., Zhang, Y., 2014. Microstructures and crackling noise of $Al_xNbTiMoV$ high entropy alloys. Entropy 16, 870–884. Chhabra, A., Jensen, R.V., 1989. Direct determination of the $f(\alpha)$ singularity spectrum. Phys. Rev. Lett. 62, 1327–1330.
- Chibane, N., Ait-Amokhtar, H., Fressengeas, C., 2017. On the strain rate dependence of the critical strain for plastic instabilities in Al-Mg alloys. Scripta Mater. 130,

252-255

- Chou, Y.L., Wang, Y.C., Yeh, J.W., Shih, H.C., 2010. The effect of molybdenum on the corrosion behaviour of the high-entropy alloys Co_{1.5}CrFeNi_{1.5}Ti_{0.5}Mo_x in aqueous environments. Corrosion Sci. 52, 1026–1034.
- Chuang, M.-H., Tsai, M.-H., Tsai, C.-W., N-H, Y., Chang, S.-Y., Yeh, J.-W., Chen, S.-K., Lin, S.-J., 2013. Intrinsic surface hardening and precipitation kinetics of Al_{0.3}CrFe_{1.5}MnNi_{0.5} multi-component alloy. J. Alloy. Comp. 551, 12–18.
- Chuang, M.-H., Tsai, M.H., Wang, W.R., Lin, S.J., Yeh, J.W., 2011. Microstructure and wear behavior of Al_xCo_{1.5}CrFeNi_{1.5}Ti_y high-entropy alloys. Acta Mater. 59, 6308-6317
- Costa, M., Goldberger, A.L., Peng, C.K., 2002. Multiscale entropy analysis of complex physiologic time series. Phys. Rev. Lett. 89, 068102.
- Costa, M., Goldberger, A.L., Peng, C.K., 2005. Multiscale entropy analysis of biological signals. Phys. Rev. 71, 021906.
- Costa, M.D., Goldberger, A.L., 2015. Generalized multiscale entropy analysis: application to quantifying the complex volatility of human heartbeat time series. Entropy 17, 1197–1203.
- Costa, M.D., Henriques, T., Munshi, M.N., Segal, A.R., Goldberger, A.L., 2014. Dynamical glucometry: use of multiscale entropy analysis in diabetes. Chaos 24 (5), 033139.
- Diao, H.Y., Feng, R., Dahmen, K.A., Liaw, P.K., 2017. Fundamental deformation behavior in high-entropy alloys: an overview. Curr. Opin. Solid State Mater. Sci. 21, 252–266.
- Egami, T., Guo, W., Rack, P.D., Nagase, T., 2014. Irradiation resistance of multicomponent alloys. Metall. Mater. Trans. 45A, 180-183.
- Field, D.M., Aken, D.C.V., 2018. Dynamic strain aging phenomena and tensile response of medium-Mn TRIP steel. Metall. Mater. Trans. 49A, 1152-1166.
- Friedman, N., Jennings, A.T., Tsekenis, G., Kim, J.-Y., Tao, M., Uhl, J.T., Greer, J.R., Dahmen, K.A., 2012. Statistics of dislocation slip avalanches in nanosized single crystals show tuned critical behavior predicted by a simple mean field model. Phys. Rev. Lett. 109, 095507 1-5.
- Gao, X., Lu, Y., Zhang, B., Liang, N., Wu, G., Sha, G., Liu, J., Zhao, Y., 2017. Microstructural origins of high strength and high ductility in an AlCoCrFeNi_{2.1} eutectic high-entropy alloy. Acta Mater. 141, 59–66.
- Glenny, R.W., Robertson, H.T., Yamashiro, S., Bassingthwaighte, J.B., 1991. Applications of fractal analysis to physiology. J. Appl. Physiol. 70, 2351–2367 Bethesda, Md.: 1985.
- Gludovatz, B., Hohenwarter, A., Catoor, D., Chang, E.H., George, E.P., Ritchie, R.O., 2014. A fracture-resistant high-entropy alloy for cryogenic applications. Science 345, 1153–1158.
- Hahner, P., Ziegenbein, A., Rizzi, E., Neuhauser, H., 2002. Spatiotemporal analysis of Portevin-Le Chatelier deformation bands: theory, simulation, and experiment. Phys. Rev. B 65 (20), 134109.
- He, M.-R., Wang, S., Jin, K., Bei, H., Yasuda, K., Matsumura, S., Higashida, K., Robertson, I.M., 2016. Enhanced damage resistance and novel defect structure of CrFeCoNi under in situ electron irradiation. Scripta Mater. 125, 5–9.
- Hemphill, M.A., Yuan, T., Wang, G.Y., Yeh, J.W., Tsai, C.W., Chuang, A., Liaw, P.K., 2012. Fatigue behavior of Al_{0.5}CoCrCuFeNi high entropy alloys. Acta Mater. 60, 5723–5734.
- Hideji, S., The Research Institute for Iron, S., Other, M., 1952. Chemical interaction of solute atoms with dislocations. Science reports of the Research Institutes, Tohoku University. Ser. A, Phys., Chem. Metall. 4, 455–463.
- Hsu, C.Y., Wang, W.R., Tang, W.Y., Chen, S.K., Yeh, J.W., 2010. Microstructure and mechanical properties of new AlCo_xCrFeMo_{0.5}Ni high-entropy alloys. Adv. Eng. Mater. 12, 44–49.
- Hu, Y., Shu, L., Yang, Q., Guo, W., Liaw, P.K., Dahmen, K.A., Zuo, J.M., 2018. Dislocation avalanche mechanism in slowly compressed high entropy alloy nanopillars. Commun. Phys. 1 (8), 61.
- Iliopoulos, A.C., Nikolaidis, N.S., Aifantis, E.C., 2015. Analysis of serrations and shear bands fractality in UFGs. J. Mech. Behav. Mater. 24, 1-9.
- Jiang, W.H., Fan, G.J., Liu, F.X., Wang, G.Y., Choo, H., Liaw, P.K., 2008. Spatiotemporally inhomogeneous plastic flow of a bulk-metallic glass. Int. J. Plast. 24, 1–16. Jo, Y.H., Jung, S., Choi, W.M., Sohn, S.S., Kim, H.S., Lee, B.J., Kim, N.J., Lee, S., 2017. Cryogenic strength improvement by utilizing room-temperature deformation twinning in a partially recrystallized VCrMnFeCoNi high-entropy alloy. Nat. Commun. 8, 15719.
- Jobba, M., Mishra, R.K., Niewczas, M., 2015. Flow stress and work-hardening behaviour of Al-Mg binary alloys. Int. J. Plast. 65, 43-60.
- Kao, Y.F., Lee, T.D., Chen, S.K., Chang, Y.S., 2017. Electrochemical passive properties of Al_xCoCrFeNi (x = 0, 0.25, 0.50, 1.00) alloys in sulfuric acids. Corrosion Sci. 52, 1026–1034.
- Koch, C.C., 2017. Nanocrystalline high-entropy alloys. J. Mater. Res. 32, 3435-3444.
- Komarasamy, M., Kumar, N., Mishra, R.S., Liaw, P.K., 2016. Anomalies in the deformation mechanism and kinetics of coarse-grained high entropy alloy. Mater. Sci. Eng. 654, 256–263.
- Kumar, N.A.P.K., Li, C., Leonard, K.J., Bei, H., Zinkle, S.J., 2016. Microstructural stability and mechanical behavior of FeNiMnCr high entropy alloy under ion irradiation. Acta Mater. 113, 230–244.
- Lan, P., Zhang, J.Q., 2018. Serrated flow and dynamic strain aging in Fe-Mn-C TWIP steel. Metall. Mater. Trans. 49A, 147-161.
- Lebedkina, T.A., Lebyodkin, M.A., 2008. Effect of deformation geometry on the intermittent plastic flow associated with the Portevin–Le Chatelier effect. Acta Mater. 56, 5567–5574.
- Lebedkina, T.A., Lebyodkin, M.A., Lamark, T.T., Janeček, M., Estrin, Y., 2014. Effect of equal channel angular pressing on the Portevin–Le Chatelier effect in an Al₃Mg alloy. Mater. Sci. Eng. 615, 7–13.
- Lebyodkin, M.A., Estrin, Y., 2005. Multifractal analysis of the Portevin-Le Chatelier effect: general approach and application to AlMg and AlMg/ Al_2O_3 alloys. Acta Mater. 53, 3403–3413.
- Lebyodkin, M.A., Kobelev, N.P., Bougherira, Y., Entemeyer, D., Fressengeas, C., Lebedkina, T.A., Shashkov, I.V., 2012. On the similarity of plastic flow processes during smooth and jerky flow in dilute alloys. Acta Mater. 60, 844–850.
- Lebyodkin, M.A., Lebedkina, T.A., 2006. Multifractal analysis of evolving noise associated with unstable plastic flow. Phys. Rev. 73 (8), 036114.
- Lebyodkin, M.A., Lebedkina, T.A., 2008. Multifractality and randomness in the unstable plastic flow near the lower strain-rate boundary of instability. Phys. Rev. 77 (8), 026111.
- Lebyodkin, M.A., Lebedkina, T.A., Jacques, A., 2009. Multifractal Analysis of Unstable Plastic Flow. Nova Science Publishers, Inc., New York.
- Lee, C., Song, G., Gao, M.C., Feng, R., Chen, P., Brechtl, J., Chen, Y., An, K., Guo, W., Poplawsky, J.D., Li, S., Samaei, A.T., Chen, W., Hu, A., Choo, H., Liaw, P.K., 2018. Lattice distortion in a strong and ductile refractory high-entropy alloy. Acta Mater. 160, 158–172.
- Li, D., Li, C.X., Feng, T., Zhang, Y.D., Sha, G., Lewandowski, J.J., Liaw, P.K., Zhang, Y., 2017a. High-entropy Al_{0.3}CoCrFeNi alloy fibers with high tensile strength and ductility at ambient and cryogenic temperatures. Acta Mater. 123, 285–294.
- Li, J.J., Wang, Z., Qiao, J.W., 2016. Power-law scaling between mean stress drops and strain rates in bulk metallic glasses. Mater. Des. 99, 427-432.
- Li, Z., Zhao, S., Diao, H., Liaw, P.K., Meyers, M.A., 2017b. High-velocity deformation of Al_{0.3}CoCrFeNi high-entropy alloy: remarkable resistance to shear failure. Sci. Rep. 7, 42742.
- Lilensten, L., Couzinie, J.-P., Perriere, L., Hocini, A., Keller, C., Dirras, G., Guillot, I., 2018. Study of a BCC multi-principal element alloy: tensile and simple shear properties and underlying deformation mechanisms. Acta Mater. 142, 131–141.
- Liu, J., Guo, X., Lin, Q., Zhanbing, H., An, X., Li, L., Liaw, P.K., Liao, X., Yu, L., Lin, J., Lu, X., Ren, J., Zhang, Y., 2019a. Excellent ductility and serration feature of metastable CoCrFeNi high-entropy alloy at extremely low temperatures. Sci. China Mater. https://doi.org/10.1007/s40843-018-9373-y.
- Liu, K.M., Komarasamy, M., Gwalani, B., Shukla, S., Mishra, R.S., 2019b. Fatigue behavior of ultrafine grained triplex Al_{0.3}CoCrFeNi high entropy alloy. Scripta Mater. 158, 116–120.
- Lyu, Z., Fan, X., Lee, C., Wang, S.-Y., Feng, R., Liaw, P.K., 2018. Fundamental understanding of mechanical behavior of high-entropy alloys at low temperatures: a review. J. Mater. Res. 33, 2998–3010.
- Maaß, R., Klaumünzer, D., Löffler, J.F., 2011. Propagation dynamics of individual shear bands during inhomogeneous flow in a Zr-based bulk metallic glass. Acta Mater. 59, 3205–3213.

Madivala, M., Schwedt, A., Wong, S.L., Roters, F., Prahl, U., Bleck, W., 2018. Temperature dependent strain hardening and fracture behavior of TWIP steel. Int. J. Plast. 104, 80–103

Meneveau, C., Sreenivasan, K.R., 1987. Simple multifractal cascade model for fully-developed turbulence. Phys. Rev. Lett. 59, 1424-1427.

Miguel, M.C., Vespignani, A., Zapperi, S., Weiss, J., Grasso, J.R., 2001. Complexity in dislocation dynamics: model. Mater. Sci. Eng. A-Struct. Mater. Prop. Microstruct. Process. 309, 324–327.

Miracle, D.B., 2017. High-entropy alloys: a current evaluation of founding ideas and core effects and exploring "nonlinear alloys. JOM 69, 2130-2136.

Miracle, D.B., Senkov, O.N., 2017. A critical review of high entropy alloys and related concepts. Acta Mater. 122, 448-511.

Nair, R.B., Arora, H.S., Mukherjee, S., Singh, S., Singh, H., Grewel, H.S., 2018. Exceptionally high cavitation erosion and corrosion resistance of a high entropy alloy. Ultrason. Sonochem. 41, 252–260.

Neuhauser, H., 1993. Collective microshear processes and plastic instabilities in crystalline and amorphous structures. Int. J. Plast. 9, 421-435.

Niu, S., Kou, H., Zhang, Y., Wang, J., Li, J., 2017. The characteristics of serration in Al_{0.5}CoCrFeNi high entropy alloy. Mater. Sci. Eng. 702, 96–103.

PastorSatorras, R., Riedi, R.H., 1996. Numerical estimates of the generalized dimensions of the Henon attractor for negative q. J. Phys. Math. Gen. 29, L391–L398. Qiao, J.W., Ma, S.G., Huang, E.W., Chuang, C.P., Liaw, P.K., Zhang, Y., 2011. Microstructural characteristics and mechanical behaviors of AlCoCrFeNi high-entropy alloys at ambient and cryogenic temperatures. In: Wang, R.M., Wu, Y., Wu, X.F. (Eds.), Nano-scale and Amourphous Materials. Trans Tech Publications Ltd, Durnten-Zurich 419+.

Rodriguez, P., 1984. Serrated plastic flow. Bull. Mater. Sci. 6, 653-663.

Salat, H., Murcio, R., Arcaute, E., 2017. Multifractal methodology. Physica A 473, 467-487.

Santodonato, L.J., Liaw, P.K., Unocic, R.R., Bei, H., Morris, J.R., 2018. Predictive multiphase evolution in Al-containing high-entropy alloys. Nat. Commun. 9, 4520. Santodonato, L.J., Zhang, Y., Feygenson, M., Parish, C.M., Gao, M.C., Weber, R.J.K., Neuefeind, J.C., Tang, Z., Liaw, P.K., 2015. Deviation from high-entropy configurations in the atomic distributions of a multi-principal-element alloy. Nat. Commun. 6, 5964.

Sarkar, A., Barat, P., Mukherjee, P., 2010. Multiscale entropy analysis of the Portevin-Le Chatelier effect in an Al-2.5%Mg alloy. Fractals 18, 319-325.

Sarkar, A., Chatterjee, A., Barat, P., Mukherjee, P., 2007. Comparative study of the Portevin-Le Chatelier effect in interstitial and substitutional alloy. Mater. Sci. Eng. A-Struct. Mater. Prop. Microstruct. Process. 459, 361–365.

Sarkar, A., Maloy, S.A., Murty, K.L., 2015. Investigation of Portevin-LeChatelier effect in HT-9 steel. Mater. Sci. Eng. 631, 120-125.

Seifi, M., Li, D., Yong, Z., Liaw, P.K., Lewandowski, J.J., 2015. Fracture toughness and fatigue crack growth behavior of as-cast high-entropy alloys. JOM 67, 2288–2295.

Sharghi-Moshtaghin, R., Asgari, S., 2008. The characteristics of serrated flow in superalloy IN738LC. Mater. Sci. Eng. A-Struct. Mater. Prop. Microstruct. Process. 486, 376–380

Shetty, M.N., 2013. Dislocations and Mechanical Behaviour of Materials. PH Learning Private Limited, New Delhi.

Shi, Y.Z., Collins, L., Balke, N., Liaw, P.K., Yang, B., 2018a. In-situ electrochemical-AFM study of localized corrosion of Al_xCoCrFeNi high-entropy alloys in chloride solution. Appl. Surf. Sci. 439, 533–544.

Shi, Y.Z., Collins, L., Feng, R., Zhang, C., Balke, N., Liaw, P.K., Yang, B., 2018b. Homogenization of Al_xCoCrFeNi high-entropy alloys with improved corrosion resistance. Corrosion Sci. 133, 120–131.

Shi, B., Luan, S.Y., Jin, P.P., 2018c. Crossover from free propagation to cooperative motions of shear bands and its effedt on serrated flow in metallic glass. J. Non-Cryst. Solids 482, 126–131.

Shi, Y., Yang, B., Xie, X., Brechtl, J., Dahmen, K.A., Liaw, P.K., 2017a. Corrosion of Al_xCoCrFeNi high-entropy alloys: Al-content and potential scan-rate dependent pitting behavior. Corrosion Sci. 119, 33–45.

Shi, Y.Z., Yang, B., Liaw, P.K., 2017b. Corrosion-Resistant high-entropy alloys: a review. Metals 7 (18), 43.

Shibkov, A.A., Gasanov, M.F., Zheltov, M.A., Zolotov, A.E., Ivolgin, V.I., 2016. Intermittent plasticity associated with the spatio-temporal dynamics of deformation bands during creep tests in an AlMg polycrystal. Int. J. Plast. 86, 37–55.

Song, Y.-Q., Liu, J.-L., Yu, Z.-G., Li, B.-G., 2015. Multifractal analysis of weighted networks by a modified sandbox algorithm. Sci. Rep. 5, 17628.

Song, Y., Xie, X., Luo, J.J., Liaw, P.K., Qi, H.R., Gao, Y.F., 2017. Seeing the unseen: uncover the bulk heterogeneous deformation processes in metallic glasses through surface temperature decoding. Mater. Today 20, 9–15.

Tabachnikova, E.D., Podolskiy, A.V., Laktionova, M.O., Bereznaia, N.A., Tikhonovsky, M.A., Tortika, A.S., 2017. Mechanical properties of the CoCrFeNiMnV_x high entropy alloys in temperature range 4.2-300 K. J. Alloy. Comp. 698, 501–509.

Tang, Z., Huang, L., He, W., Liaw, P.K., 2014. Alloying and processing effects on the aqueous corrosion behavior of high-entropy alloys. Entropy 16, 895–911.

Tang, Z., Yuan, T., Tsai, C.W., Yeh, J.W., Lundin, C.D., Liaw, P.K., 2015. Fatigue behavior of a wrought Al_{0.5}CoCrCuFeNi two-phase high-entropy alloy. Acta Mater. 99, 247–258

Thurston, K.V.S., Gludovatz, B., Hohenwarter, A., Laplanche, G., George, E.P., Ritchie, R.O., 2017. Effect of temperature on the fatigue-crack growth behavior of the high-entropy alloy CrMnFeCoNi. Intermetallics 88, 65–72.

Tong, C.J., Chen, M.R., Chen, S.K., Yeh, J.W., Shun, T.T., Lin, S.J., Chang, S.Y., 2005. Mechanical performance of the Al_xCoCrCuFeNi high-entropy alloy system with multiprincipal elements. Mater. Sci. Eng. A-Struct. Mater. Prop. Microstruct. Process. 36A, 1263–1271.

Torre, F.H.D., Klaumünzer, D., Maaß, R., Löffler, J.F., 2010. Stick-slip behavior of serrated flow during inhomogeneous deformation of bulk metallic glasses. Acta Mater. 58, 3742–3750.

Uhl, J.T., Pathak, S., Schorlemmer, D., Liu, X., Swindeman, R., Brinkman, B.A.W., LeBlanc, M., Tsekenis, G., Friedman, N., Behringer, R., Denisov, D., Schall, P., Gu, X., Wright, W.J., Hufnagel, T., Jennings, A., Greer, J.R., Liaw, P.K., Becker, T., Dresen, G., Dahmen, K.A., 2015. Universal quake statistics: from compressed nanocrystals to earthquakes. Sci. Rep. 5, 16493.

Valdes-Tabernero, M.A., Sancho-Cadenas, R., Sabirov, I., Murashkin, M.Y., Ovid'ko, I.A., Galvez, F., 2017. Effect of SPD processing on mechanical behavior and dynamic strain aging of an Al-Mg alloy in various deformation modes and wide strain rate range. Mater. Sci. Eng. 696, 348–359.

Weiss, J., Grasso, J.R., Miguel, M.C., Vespignani, A., Zapperi, S., 2001. Complexity in dislocation dynamics: experiments. Mater. Sci. Eng. A-Struct. Mater. Prop. Microstruct. Process. 309, 360–364.

Wu, S.-D., Wu, C.-W., Lin, S.-G., Lee, K.-Y., Peng, C.-K., 2014. Analysis of complex time series using refined composite multiscale entropy. Phys. Lett. 378, 1369–1374. Xia, S.-Q., Wang, Z., Yang, T.-F., Zhang, Y., 2015a. Irradiation behavior in high entropy alloys. J. Iron Steel Res. 22, 879–884.

Xia, S., Gao, M.C., Yang, T., Liaw, P.K., Zhang, Y., 2016. Phase stability and microstructures of high entropy alloys ion irradiated to high doses. J. Nucl. Mater. 480, 100–108.

Xia, S.Q., Yang, X., Yang, T.F., Liu, S., Zhang, Y., 2015b. Irradiation resistance in Al_xCoCrFeNi high entropy alloys. JOM 67, 2340–2344.

Yang, F., Luo, H.W., Pu, E.X., Zhang, S.L., Dong, H., 2018a. On the characteristics of Portevin-Le Chatelier bands in cold-rolled 7Mn steel showing transformation induced plasticity. Int. J. Plast. 103, 188–202.

Yang, T., Xia, S., Guo, W., Hu, R., Poplawsky, J.D., Sha, G., Fang, Y., Yan, Z., Wang, C., Li, C., Zhang, Y., Zinkle, S.J., Wang, Y., 2018b. Effects of temperature on the irradiation responses of Al_{0.1}CoCrFeNi high entropy alloy. Scripta Mater. 144, 31–35.

Yang, T., Xia, S., Liu, S., Wang, C., Liu, S., Fang, Y., Zhang, Y., Xue, J., Yan, S., Wang, Y., 2016. Precipitation behavior of Al_xCoCrFeNi high entropy alloys under ion irradiation. Sci. Rep. 6, 32146.

Yasuda, H.Y., Shigeno, K., Nagase, T., 2015. Dynamic strain aging of Al_{0.3}CoCrFeNi high entropy alloy single crystals. Scripta Mater. 108, 80–83.

Yeh, J.W., Chen, S.K., Gan, J.Y., Lin, S.J., Chin, T.S., Shun, T.T., Tsau, C.H., Chang, S.Y., 2004a. Formation of simple crystal structures in Cu-Co-Ni-Cr-Al-Fe-Ti-V alloys with multiprincipal metallic elements. Mater. Sci. Eng. A-Struct. Mater. Prop. Microstruct. Process. 35A, 2533–2536.

Yeh, J.W., Chen, S.K., Lin, S.J., Gan, J.Y., Chin, T.S., Shun, T.T., Tsau, C.H., Chang, S.Y., 2004b. Nanostructured high-entropy alloys with multiple principal elements: novel alloy design concepts and outcomes. Adv. Eng. Mater. 6, 299–303.

Yilmaz, A., 2011. The Portevin-Le Chatelier effect: a review of experimental findings. Sci. Technol. Adv. Mater. 12 (16), 063001.

Yoshinaga, H., Morozumi, S., 1971. Portevin-Le Chatelier effect expected from solute atmosphere dragging. Phil. Mag. 23, 1351-1366.

- Yuzbekova, D., Mogucheva, A., Zhemchuzhnikova, D., Lebedkina, T., Lebyodkin, M., Kaibyshev, R., 2017. Effect of microstructure on continuous propagation of the Portevin-Le Chatelier deformation bands. Int. J. Plast. 96, 210-226.
- Zavattieri, P.D., Savic, V., Hector, L.G., Fekete, J.R., Tong, W., Xuan, Y., 2009. Spatio-temporal characteristics of the Portevin-Le Chatelier effect in austenitic steel with twinning induced plasticity. Int. J. Plast. 25, 2298–2330.
 Zhang, Y., Liu, J.P., Chen, S.Y., Xie, X., Liaw, P.K., Dahmen, K.A., Qiao, J.W., Wang, Y.L., 2017. Serration and noise behaviors in materials. Prog. Mater. Sci. 90,
- 358-460.
- Zhang, Y., Stocks, G.M., Jin, K., Lu, C., Bei, H., Sales, B.C., Wang, L., Béland, L.K., Stoller, R.E., Samolyuk, G.D., Caro, M., Caro, A., Weber, W.J., 2015. Influence of chemical disorder on energy dissipation and defect evolution in concentrated solid solution alloys. Nat. Commun. 6, 8736.
- Zhang, Y., Zuo, T.T., Tang, Z., Gao, M.C., Dahmen, K.A., Liaw, P.K., Lua, Z.P., 2014. Microstructures and properties of high-entropy alloys. Prog. Mater. Sci. 61, 1–93.